

A far-infrared molecular and atomic line survey of the Orion KL region.

M.R. Lerate,^{1,2} M.J. Barlow,¹ B.M. Swinyard,² J.R. Goicoechea,³
J. Cernicharo,⁴ T.W. Grundy,² T.L. Lim,² E.T. Polehampton,² J.P. Baluteau,⁵
S. Viti,¹ and J. Yates¹

¹ *University College London, Gower Street, London WC1E 6BT, U.K*

² *Rutherford Appleton Laboratory, Chilton, Didcot OX11 0QX, U.K*

³ *LERMA, UMR 8112, CNRS, Observatoire de Paris and Ecole Normale Supérieure, 24 Rue Lhomond 75231 Paris Cedex 05, France*

⁴ *CSIC, Instituto de Estructura de la Materia, Serrano 121, 28006 Madrid, Spain.*

⁵ *Laboratoire d'Astrophysique de Marseille, CNRS & Université de Provence, BP-8, F-13376 Marseille Cedex, France*

Released 2005 Xxxxx XX

ABSTRACT

We have carried out a high spectral resolution ($\lambda/\Delta\lambda \sim 6800 - 9700$) line survey towards the Orion Kleinmann-Low (KL) cluster from 44–188 μm . The observations were taken with the Long Wavelength Spectrometer (LWS) in Fabry-Pérot mode, on board the *Infrared Space Observatory (ISO)*. A total of 152 lines are clearly detected and a further 34 features are present as possible detections. The spectrum is dominated by the molecular species H_2O , OH and CO, along with [O I] and [C II] lines from PDR or shocked gas and [O III], [N III] lines from the foreground M42 H II region. Several isotopic species, as well as NH_3 , are also detected. HDO and H_3O^+ are tentatively detected for the first time in the far-infrared range towards Orion-KL. A basic analysis of the line observations is carried out, by comparing with previous measurements and published models and deriving rotational temperatures and column densities in the case of the molecular species.

Analysis of the [O I] and [C II] fine structure lines indicates that although a shock model can reproduce the observed [O I] surface brightness levels, it falls short of the observed [C II] level by more than a factor of 30. A PDR model can reproduce the [O I] 63.2 μm and [C II] surface brightness levels within 35%, although over-predicting the LWS [O I] 145.5 μm emission by a factor of 2.7. The 70 water lines and 22 OH lines detected by the survey appear with mainly P Cygni profiles at the shortest survey wavelengths and with mainly pure emission profiles at the longest survey wavelengths. The emission and absorption velocity peaks of the water and OH lines indicate that they are associated with gas expanding in the outflow from the KL cluster. The estimated column densities are $(2\text{--}5)\times 10^{14} \text{ cm}^{-2}$ for H_2O and $(2.5\text{--}5.1)\times 10^{16} \text{ cm}^{-2}$ for OH. The 26 detected CO lines confirm the presence of three distinct components, with temperature and column density combinations ranging from 660 K, $6\times 10^{17} \text{ cm}^{-2}$ to 360 K, $2\times 10^{19} \text{ cm}^{-2}$. Comparison of the surface brightnesses and integrated fluxes of the CO lines measured in the 80-arcsec LWS beam with those measured previously by the *Kuiper Airborne Observatory (KAO)* in a 44 arcsec beam shows similar surface brightnesses in the different beams for the lowest-J CO lines and similar integrated fluxes in the different beams for the highest-J CO lines, indicating that emission from the former lines has a uniform surface brightness within the LWS beam, while the latter lines originate from a region less than 44 arcsec in diameter. The complexity of the region requires more sophisticated models for the interpretation of all the line observations.

Key words: infrared: ISM – ISM: molecules – ISM: individual (Orion) – surveys – line: identification – ISM: lines and bands

1 INTRODUCTION

The formation of a star is often associated with outflows which can compress and heat the surrounding quiescent gas, altering the chemistry of the parent molecular cloud in which the star is forming. Many of the molecules responsible for cooling the gas in these molecular clouds, such as CO ($J \geq 14$), OH and H₂O, emit at far-infrared wavelengths ($> 40\mu\text{m}$) which are difficult to detect from the ground due to the constraints of the Earth's atmosphere. The launch of ESA's *Infrared Space Observatory (ISO)* in 1995 marked a revolution in our ability to observe these transitions, and in particular, opened a window for large-scale high resolution far-infrared spectroscopy of star forming regions such as Orion. In this paper we report on the first, and to date only, unbiased high spectral resolution spectral survey in the far-infrared waveband of the Kleinmann-Low (KL) region of Orion and discuss the implications of the results for the interpretation of the chemical evolution of the region.

The Orion star-forming complex, at a distance of 450 pc, is our nearest region of high mass star formation. It mainly consists of two giant molecular clouds: Orion molecular clouds 1 and 2 (OMC1 and OMC2), which were revealed via large scale mapping in the $J=1 \rightarrow 0$ ¹²CO rotational transition (Tucker, Kutner & Thaddeus, 1973). OMC1 is associated with the dark clouds L1640, L1641, L1647 (Lynds 1962), extending over 6° southwards from the Orion nebula. The OMC1 ridge is associated with regions of prominent molecular emission, with the region near the Orion Nebula being the best studied example. OMC1 contains the visible nebula M42, a blister of hot, photo-ionised luminous gas around the hot Trapezium stars (see Figure 1) and also contains a number of IR-emitting regions such as the Kleinmann-Low nebula, which is the brightest far-infrared region in the complex (Kleinmann & Low 1967). The KL nebula includes an infrared cluster of massive stars at an early evolutionary stage, e.g. the Becklin-Neugebauer object (BN, Becklin & Neugebauer 1967) and IRC2, which dominate the mid-infrared radiation (Downes et al. 1981). There are at least two molecular outflows, one associated with material ejected at hundreds of km s^{-1} forming a bipolar cone of molecular fingers, whose axis is perpendicular to the NH₃ emission associated with the hot core (Wilson et al. 2000), and a second low-velocity outflow first detected by H₂O maser observations (Genzel et al. 1981). IRC2 was originally believed to be the major source of the KL luminosity ($L \sim 10^5 L_\odot$, Genzel & Stutzki, 1989). However, the infrared observations of Dougados et al. (1993) resolved IRC2 into four components which may not even be self-luminous, and radio studies located the origin of the outflow as being offset by 0.5 arcsec from IRC2-A; at the position of radio source I (Menten & Reid 1995, Gezari et al. 1998, Chandler & Greenhill 2002).

Within the KL region, molecular emission arises from several physically distinct regions:

- The Hot Core is composed of very dense material with $n \sim 10^7 \text{ cm}^{-3}$ and $T \sim 200\text{K}$ in clumps located $\sim 2''$ south of IRC2, $1''$ offset from radio source I (Wright et al. 1996, Schilke et al. 2001).
- The Compact Ridge is a compact region ($14''$) of dense gas ($n \sim 10^6 \text{ cm}^{-3}$) surrounded by outflows.

- The Plateau; a region of inhomogeneous density containing both low-velocity ($\sim 18 \text{ km s}^{-1}$) and high-velocity ($\sim 100 \text{ km s}^{-1}$) flows with an approximate diameter of $50''$ (Blake et al. 1987).

- Finally the whole region is embedded in the Extended Ridge, a region of quiescent and cooler gas from which many narrow lines ($\Delta v \sim 3\text{--}5 \text{ km s}^{-1}$ FWHM) are detected (Greaves & White 1991).

The proximity and complexity of the KL region have made it the target of many astronomical studies, and it is one of the best studied examples of the interaction between massive stars in their earliest stages and their parental molecular cloud. In this paper we report the results of an unbiased spectral survey between $44\text{--}188\mu\text{m}$ (1612 to 6813 GHz) at a resolving power of ≈ 8000 , which represents the first systematic study of the molecular spectrum in this wavelength range. A number of the detected lines from this spectral survey and from a series of targeted observations have already been reported (e.g. the OH lines; Goicoechea et al. 2006, some H₂O lines; Harwit et al. 1998, Cernicharo et al. 1999, and some CO lines Sempere et al. 2000), however, this is the first analysis of the entire spectrum.

Our spectral survey provides an insight into the physical conditions and dynamical processes in the Orion KL region and complements studies performed at lower frequencies, e.g. from 72 to 91 GHz (Johansson et al. 1984), 70 to 115 GHz (Turner 1989), 150 to 160 GHz (Ziurys & McGonagle 1993), 215 to 247 GHz (Sutton et al. 1985), 247 to 263 GHz (Blake et al. 1986) 325 to 360 GHz (Schilke et al. 1997), 455 to 507 GHz (White et al. 2003), 607 to 725 GHz (Schilke et al. 2001) and 795 to 903 GHz (Comito et al. 2005).

The aim of this work is to present the data, describe its reduction and calibration and discuss some basic results. Section 2 describes the observations and data reduction, including a brief summary of the instrumental operation. Section 3 presents the results, while the individual species are discussed in Section 4. Our results are summarised in Section 5.

2 OBSERVATIONS AND DATA REDUCTION

2.1 Instrumental operation

The Long Wavelength Spectrometer (LWS; Clegg et al. 1996) was one of the four instruments on board the *Infrared Space Observatory (ISO)*, which operated between November 1995 and April 1998, when the superfluid helium used to cool the instruments ran out. The LWS covered the spectral range between 43 and $197\mu\text{m}$ at medium resolution ($\lambda/\Delta\lambda \sim 150\text{--}200$) using a diffraction grating and at high resolution ($\lambda/\Delta\lambda \sim 6800\text{--}9700$) with one of two Fabry-Pérot (FP) etalons, order sorted by the grating. Four different observing modes were available to users, via the so-called 'Astronomical Observation Templates' (AOTs), which allowed the observer a choice of wavelength ranges, sampling intervals and exposure times. These observing modes were: medium resolution, full wavelength range spectrum (AOT L01), medium resolution and narrow band photometry, selected wavelength range spectrum (AOT L02), high-resolution, full wavelength range (AOT L03) and high-resolution, narrow wavelength range (AOT



Figure 1. Colour composite mosaic image of the central part of the Orion Nebula, M42, based on 81 images obtained with the infrared multi-mode ISAAC instrument on the ESO Very Large Telescope (VLT) at the Paranal Observatory. The Trapezium stars are seen near the centre (ESO PR Photo 03a/01 2001).

L04). Also, a parallel mode was carried out while an AOT was active with another instrument and a serendipity mode was carried out during the slews with no prime instrument. Since a full spectral scan with the LWS FP (AOT L03) took a long time, a significant part of the spectrum was recorded at high spectral resolution for only four objects: Orion BN/KL, Sgr B2 (Polehampton 2002, Polehampton et al. 2006 in prep.), Sgr A and Jupiter.

In L03 mode, data for a given wavelength range were recorded by scanning the FP gap over a small range with the grating held stationary, thus shifting the wavelength of the selected FP order across the grating response function. To record data for another wavelength range the grating was moved by a portion of the grating resolution element and the FP scanned again: the data set recorded at each grating setting is termed a *mini-scan*.

During each observation the LWS FP and grating settings were optimised for the detector whose band pass filter included the wavelength range of interest. This was denoted as the ‘prime’ detector. However, all ten LWS detectors recorded data simultaneously in their own spectral ranges; the other detectors are termed ‘non-prime’.

2.2 Observations

The observations were carried out between September 1997 and April 1998. The dataset consists of 26 individual observations making up a total of 27.9 hours of *ISO* LWS observing time in L03 mode, 16 observations making up 13.1 hours in L04 mode and 1 observation in the lower resolution L01 grating mode. The instrumental field of view for all L03 observations was either centred on a position offset by $10.5''$ from the BN object (which is at $05^{\text{h}} 35^{\text{m}}$

$14.12^{\text{s}} - 05^{\circ} 22' 22.9''$ J2000), or a position offset by $5.4''$ from IRc2 (which is at $05^{\text{h}} 35^{\text{m}} 14.45^{\text{s}} - 05^{\circ} 22' 30.0''$ J2000) while most of the L04 observations were centred on IRc2 (see Table 1 and Figure 2). The LWS beam had a diameter $\approx 80''$ (Gry et al. 2003). Table 1 lists the observations: column one is the Target Dedicated Time identification number (TDT). The TDT is an eight digit number unique to each observation; the first three digits are the *ISO* revolution number, the next three digits are the sequence number of the observation in the revolution and the last two numbers were assigned by the observer. Column two lists the wavelength range covered by the prime detector. The length of the observation in seconds can be found in column three while the observation date (d.m.y) is in column four. The J2000 coordinates of the pointing position for each observation can be found in columns five and six respectively.

2.3 Data reduction

Processing of the LWS FP data was carried out using the Offline Processing (OLP) pipeline and the LWS Interactive Analysis (LIA) package version 10. The basic calibration is fully described in the LWS handbook (Gry et al. 2003). Further processing, including dark current optimisation, de-glitching and removal of the LWS grating profile was then carried out interactively using the LWS Interactive Analysis package version 10 (LIA10; Lim et al. 2002) and the *ISO* Spectral Analysis Package (ISAP; Sturm 1998). The reduction process was performed in the same way as that for the *ISO* L03 Sagittarius B2 data (Polehampton et al. 2006 in prep) with the only exception being the *mini-scan* shape removal (see below). The dataset contains data from both prime and non-prime detectors.

Detector dark currents were determined during the mission by three different methods (Swinyard et al. 1998). Table 2 lists the nominal dark current, which is the average of these measurements. However, scattering of light into the detectors may have occurred during observations of extended or off-axis sources. This could contribute an additional component to the dark signal which varied from source to source and is not easy to distinguish from the detector dark current or the source signal. A method to determine both the dark current and stray light corrections for a particular observation was developed by Polehampton (2002) using non-prime data from the observation of Sagittarius B2 (see also Polehampton et al. 2006). The method is based on the fact that for some *mini-scans* the transmitted orders from the FP do not correspond to the wavelength range transmitted by the grating. In these circumstances no light was transmitted and the detector will have recorded only the dark current and the stray light that finds its way to the detectors from outside of the main beam - the dark signal.

This method was used on the Orion data and dark signal corrections were applied via the graphical interface available in the LIA interactive reduction package. Table 2 lists the values of the dark signal that were subtracted from the observations for each detector compared to the ‘nominal’ dark current.

Basic removal of the *mini-scan* shape was also performed interactively in the LIA. Any remaining *mini-scan* residual

TDT	Wavelength(μm)	length(s)	Date	J2000 RA	J2000 Dec
AOT = L03					
66302402	47–52	5586	9.9.97	5 ^h 35 ^m 14 ^s .17	-5° 22' 33''.5
66302406	47–52	5586	9.9.97	5 ^h 35 ^m 14 ^s .17	-5° 22' 33''.5
66002003	52–57	4434	6.9.97	5 ^h 35 ^m 14 ^s .17	-5° 22' 33''.4
66002007	52–57	4434	6.9.97	5 ^h 35 ^m 14 ^s .17	-5° 22' 33''.4
70101704	57–63	5726	17.10.97	5 ^h 35 ^m 14 ^s .17	-5° 22' 33''.8
70101708	57–63	5726	17.10.97	5 ^h 35 ^m 14 ^s .17	-5° 22' 33''.8
70001205	63–70	5641	16.10.97	5 ^h 35 ^m 14 ^s .17	-5° 22' 33''.8
70001209	63–70	5642	16.10.97	5 ^h 35 ^m 14 ^s .17	-5° 22' 33''.8
69901510	70–73	2592	15.10.97	5 ^h 35 ^m 14 ^s .17	-5° 22' 33''.8
69901514	70–73	2591	15.10.97	5 ^h 35 ^m 14 ^s .17	-5° 22' 33''.8
69901312	77–81	4106	15.10.97	5 ^h 35 ^m 14 ^s .17	-5° 22' 33''.8
69901316	77–81	4106	15.10.97	5 ^h 35 ^m 14 ^s .17	-5° 22' 33''.8
69901413	81–85	3842	15.10.97	5 ^h 35 ^m 14 ^s .17	-5° 22' 33''.8
69901417	81–85	3842	15.10.97	5 ^h 35 ^m 14 ^s .17	-5° 22' 33''.8
70001105	85–89	2530	15.10.97	5 ^h 35 ^m 14 ^s .16	-5° 22' 33''.7
70001127	85–89	2530	16.10.97	5 ^h 35 ^m 14 ^s .17	-5° 22' 33''.8
87301008	99–104	2924	6.4.98	5 ^h 35 ^m 14 ^s .15	-5° 22' 33''.4
87301030	99–104	2924	6.4.98	5 ^h 35 ^m 14 ^s .15	-5° 22' 33''.4
87300909	104–109	2748	6.4.98	5 ^h 35 ^m 14 ^s .15	-5° 22' 33''.4
87300931	104–109	2748	6.4.98	5 ^h 35 ^m 14 ^s .15	-5° 22' 33''.4
82702210	109–115	3226	19.2.98	5 ^h 35 ^m 14 ^s .15	-5° 22' 33''.5
82702232	109–115	3226	20.2.98	5 ^h 35 ^m 14 ^s .15	-5° 22' 33''.5
84101911	115–121	3140	5.3.98	5 ^h 35 ^m 14 ^s .15	-5° 22' 33''.4
84101933	115–121	3140	5.3.98	5 ^h 35 ^m 14 ^s .15	-5° 22' 33''.5
82602316	147–154	3830	18.2.98	5 ^h 35 ^m 14 ^s .15	-5° 22' 33''.5
82602338	147–154	3830	18.2.98	5 ^h 35 ^m 14 ^s .15	-5° 22' 33''.5
AOT = L04					
83101203	51–101	2166	23.02.98	5 ^h 35 ^m 14 ^s .45	-5° 22' 30''.0
69000714	51–125	6918	06.10.95	5 ^h 35 ^m 14 ^s .21	-5° 22' 23''.5
82901207	54–75	1818	22.02.98	5 ^h 35 ^m 14 ^s .45	-5° 22' 30''.0
82901101	68–129	3858	21.02.98	5 ^h 35 ^m 14 ^s .45	-5° 22' 29''.5
69602606	70–124	2334	12.10.97	5 ^h 35 ^m 14 ^s .47	-5° 22' 29''.8
69602605	73–180	2028	12.10.9	5 ^h 35 ^m 14 ^s .47	-5° 22' 29''.8
82901206	75–94	1772	21.02.98	5 ^h 35 ^m 14 ^s .45	-5° 22' 30''.1
83101202	83–180	2282	23.02.98	5 ^h 35 ^m 14 ^s .45	-5° 22' 30''.1
70101216	84–179	3028	17.10.97	5 ^h 35 ^m 14 ^s .47	-5° 22' 30''.4
83101201	96–180	2416	23.02.98	5 ^h 35 ^m 14 ^s .45	-5° 22' 30''.1
69602317	100–180	1980	12.10.97	5 ^h 35 ^m 14 ^s .47	-5° 22' 30''.4
82901204	105–146	1630	21.02.98	5 ^h 35 ^m 14 ^s .45	-5° 22' 30''.1
83101301	119–120	3380	23.02.98	5 ^h 35 ^m 14 ^s .49	-5° 22' 30''.9
68701716	119–165	7661	03.10.97	5 ^h 35 ^m 14 ^s .21	-5° 22' 23''.5
69602318	119–179	2492	12.10.97	5 ^h 35 ^m 14 ^s .48	-5° 22' 30''.4
68701301	148–152	1294	03.10.97	5 ^h 35 ^m 14 ^s .47	-5° 22' 29''.8

Table 1. List of all L03 and L04 observations centred on Orion IRc2-BN/KL analysed in this work. Observations are sorted by wavelength range covered by the prime detector. Note that for L04 spectra, only certain targeted observations were covered in the quoted wavelength range.

shape is due to incorrect subtraction of the grating response profile as a consequence of a positional uncertainty in the absolute grating position. The effect can be seen as periodic structures in regions where *mini-scans* overlap. These features are very difficult to remove being still present in the final LIA product. Therefore, a further step was performed for the Orion data by using smooth functions and removing the residuals individually for every *mini-scan* (see also following section).

The Orion KL region was also observed using the grating in L01 mode in revolution 695. Due to the strength of the source, the grating data had to be corrected for the effects of

detector saturation (Leeks et al. 1999). Channel fringing and spurious features introduced by the Relative Spectral Response Function (RSRF) were also corrected by using the Highly Processed Data Products (HPDP) available in the *ISO* data archive (Lloyd et al. 2003). The final L01 product has a superior flux calibration accuracy compared to the FP data and was therefore used to derive the continuum level. As part of the normalisation process, FP data were first smoothed to the same resolution as the grating, using a bin size of 0.07 μm for the SW detectors and 0.15 μm for the LW detectors. Finally, each FP spectrum was corrected to

Detector	Nominal dark current ($\times 10^{-16}$ A)	FPS ($\times 10^{-16}$ A)	FPL ($\times 10^{-16}$ A)
SW1	4.96 ± 0.55		
SW2	2.08 ± 0.43	6.10 ± 0.20	
SW3	2.20 ± 0.21	4.97 ± 0.19	
SW4	1.18 ± 0.34	2.41 ± 0.11	5.48 ± 0.49
SW5	1.56 ± 0.24	2.11 ± 0.06	5.75 ± 0.56
LW1	2.50 ± 0.29	3.80 ± 0.15	4.20 ± 0.07
LW2	0.07 ± 0.27	1.03 ± 0.05	4.64 ± 0.06
LW3	0.53 ± 0.39	2.01 ± 0.42	4.83 ± 0.35
LW4	1.76 ± 0.42	4.41 ± 0.65	5.28 ± 0.28
LW5	1.21 ± 0.25	1.49 ± 0.14	1.47 ± 0.06

Table 2. Nominal dark currents adopted in the standard pipeline processing for OLP version 10 (column one) and averaged values of the dark current and stray light correction determined for the Orion dataset for the two FPs.

the Local Standard of Rest velocity (LSR) using the Starlink routine RV (Wallace & Clayton 1996).

2.4 Spectrum reliability, signal to noise achieved

After the dark current optimization and *mini-scan* shifting many spurious features were observed in the data. These structures can be easily recognized and divided into two different types: features due to *mini-scans* shifting, and features transferred via the Relative Spectral Response Function (RSRF) in the calibration stage. The first are introduced by the fact that each observation is built up of *mini-scans* and interactively adjusted as part of the reduction process.

This residual shape is difficult to remove, especially for short wavelength detectors and an alternative method was used to minimize transferred features. For each *mini-scan* a smooth function was fitted and used to remove the *mini-scan* shape. This method significantly improved the signal to noise achieved but introduced an error due to the fact that each observation is divided by the flux level achieved in each particular *mini-scan*. This means that the same lines recorded in different observations could present a slight difference in flux level in the final reduced file. However, the difference in flux when the same spectral range was observed by two adjacent detectors was found to be relatively small (see Figure 3), introducing errors of less than 20%.

The second group of features are transferred from the calibration via the RSRF and are probably caused by transient effects in the detectors. They can be seen as large scale features.

The overall signal to noise achieved in the survey as a function of wavelength is shown in Figure 4. The inclusion of non-prime data fills in some gaps in spectral coverage that were present in the prime data as well as overlapping in some places with the prime observations. This improves the signal to noise achieved by a factor that depends on the detector. Polehampton et al. (2006 in prep.) give a detailed explanation of the effect of including non-prime data on the overall signal to noise, based on the throughput of the LWS

FP etalons.

High spectral resolution can provide detailed information as a function of velocity for atomic and molecular transitions as well as unique information about the temperature and density regimes in which the transitions occur. Information on dynamical processes can be inferred by comparing line shapes; this can be easily seen for Orion KL, with H₂O and OH lines showing pure absorption, P-Cygni and pure emission profiles (see Section 4).

The advantages of high resolution spectroscopy can be seen by comparing the same wavelength region observed in the low resolution (L01) and high resolution (L03) mode. Figure 5 shows a section of the low spectral resolution observation (L01 mode) compared with the high spectral resolution (L03 mode) scan of the same region. At least 80% of the lines detected in the L03 scan are missed in the lower resolution spectrum.

2.5 The LWS Beam profile

The LWS beam profile is the convolution of the telescope point spread function (PSF) with the aperture of each detector. Ideally, the telescope PSF should be an Airy profile but the central obscuration, secondary supports and any optical imperfections redistribute power from the core of the profile to the Airy rings (Gry et al. 2003). The latest model of the telescope PSF (Gry et al. 2003) includes the effects of the central obscuration and its supporting structure, and indicates that the power in the Airy rings is increased and that the wings of the profile contain 2D asymmetric structure. The asymmetry introduced into the profile is due to the three-legged secondary support. The aperture was assumed to be circular with a top hat profile (Gry et al. 2003, Lloyd et al. 2003). Table 3 lists the effective diameter of the aperture of each detector used to derive the effective solid angle. The solid angle is defined as $2\pi(1 - \cos \theta)$, where θ is the effective beam angular radius.

2.6 Line flux measurements

The shape of the FP spectral response function was determined from dedicated calibration observations of narrow,

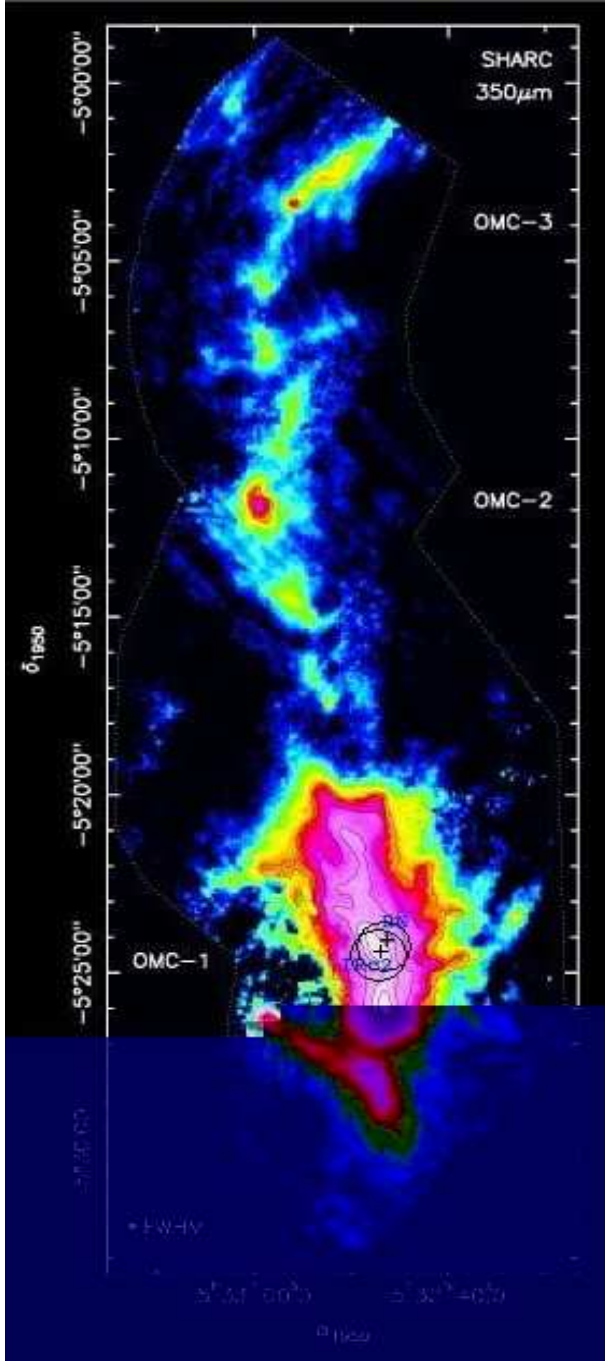


Figure 2. Approximate LWS observation center (cross points) at the positions of IRC2 and 10.5'' offset from the BN object on a false colour-image from Lis et al. (1998) showing the 350 μm continuum emission observed with SHARC. (Courtesy of D. Lis). The circles show the LWS beam positions.

unresolved spectral lines in the spectra of planetary nebula. These observations show that the response function shape can be accurately described by the predicted (Hecht and Zajac, 1974) Airy profile. The observed line profile is then the convolution of the source intrinsic profile with the Airy function. Line measurements were done by fitting a Lorentzian profile using the interactive line-fitting routine in ISAP. The Lorentzian function was found to approximate the line shape

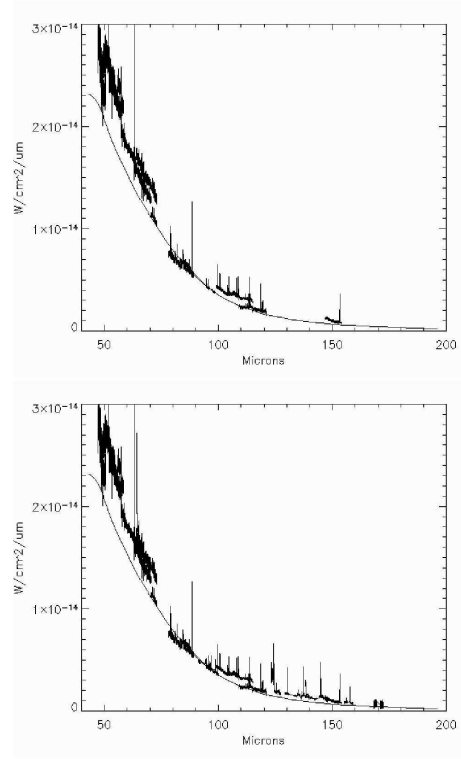


Figure 3. All L03 prime observations (upper plot) and non-prime observations (down plot) together with a continuum fit to the grating observations. Note that for wavelengths $\geq 120 \mu\text{m}$ the spectrum is mainly covered by non-prime data.

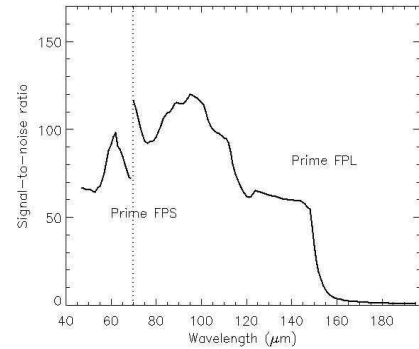


Figure 4. The signal to noise achieved for the L03 prime-detector spectra. Peaks in the curve represent the spectral ranges with the highest data reliability. The vertical dotted line divides the spectral ranges observed by the short wavelength FP (FPS) from those observed by the long wavelength FP (FPL)

very well, however, for unidentified features and lines with poor signal, a Gaussian fitting function was selected. Data were averaged over detectors and scans. The ISAP fitting procedure gives the line flux, line centre, FWHM, and an estimate of the statistical error on the line flux.

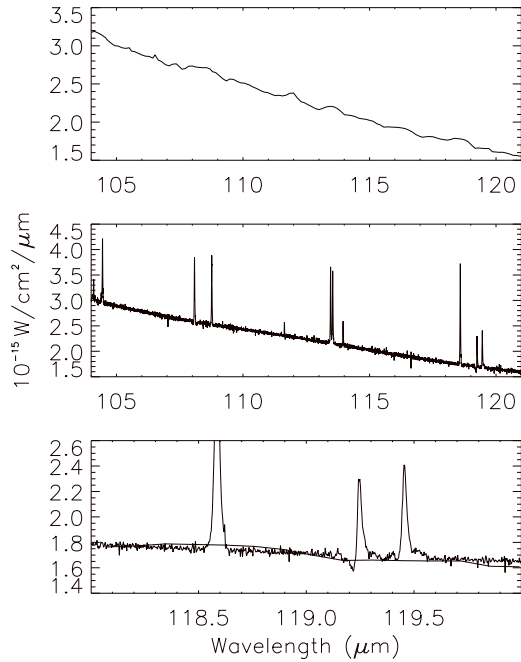


Figure 5. Comparison of a section of the low resolution L01 spectrum of Orion KL (top plot) with the high resolution L03 spectrum (middle plot). The bottom plot shows a direct comparison of the two spectra in a narrower spectral range.

Detector	Wavelength range (μm)	Effective radius ($''$)	Effective solid angle (sr)
SW1	43-50.5	39.4	1.15×10^{-7}
SW2	49.5-64	42.3	1.32×10^{-7}
SW3	57-70	43.5	1.40×10^{-7}
SW4	67-82	40.9	1.23×10^{-7}
SW5	76-93	39.5	1.15×10^{-7}
LW1	84-110	38.6	1.10×10^{-7}
LW2	103-128	38.9	1.12×10^{-7}
LW3	123-152	35.5	9.30×10^{-8}
LW4	142-171	34.7	8.89×10^{-8}
LW5	167-197	33.2	8.14×10^{-8}

Table 3. The effective beam radius and effective solid angle subtended by each detector. Differences in effective apertures are due to asymmetries introduced into the profile by the three-legged secondary instrumental support (Gry et al. 2003)

3 DATA ANALYSIS AND RESULTS

Line identification was carried out based on the JPL line catalogue (Pickett et al. 1998) and the molecular catalogue created and maintained by one of us (JC), which includes more than 1200 molecular species. The spectrum is dominated by molecular lines of CO, OH and H₂O and by forbidden lines of [O III], [O I], [N III], [N II] and [C II]. Isotopic variants and the lowest transitions of HDO, NH₃ and H₃O⁺

are also detected. Table 4 and Figure 6 show the identified lines.

4 DISCUSSION OF INDIVIDUAL SPECIES

A basic analysis and discussion of the individual detected species is presented in the following sub-sections.

From the analysis of the atomic forbidden lines, we derive physical parameters such as temperatures and densities by comparing our measurements with models. When conditions are appropriate, we use the ‘rotation diagram’ method to determine molecular parameters such as rotation temperatures and column densities. A problem with using the rotational diagram method is that it underestimates the total column density if the energy distribution is far from Local Thermodynamic Equilibrium (LTE). In order to decide whether the use of this method is appropriate, we estimated line optical depths using the statistical equilibrium radiative transfer code RADEX. (Schoier et al. 2005). RADEX is a one-dimensional non-LTE radiative transfer code that uses the escape probability formulation assuming an isothermal and homogeneous medium without large-scale velocity fields.

4.1 Atomic forbidden Lines

Table 5 lists several detected forbidden transitions observed by the survey: [O III] 52 μm , 88 μm , [N III] 57 μm , [N II] 122 μm , [O I] 63 μm , 145 μm and [C II] 158 μm . The flux errors were deduced from Lorentzian profile fitting (except the [N II] 122 μm line) and do not include systematic errors caused by uncertainties in the flux calibration, see Section 2.4. The [N II] 122 μm line was fitted using a Gaussian profile due to its width and low intensity. This broadness is due to hyperfine components in the transition as can be seen in the detection of the [N II] 122 μm line in Sgr B2 (Polehampton et al. 2006, in prep.).

4.1.1 Lines from ionised gas: [O III], [N III] and [N II]

The [O III] 52, 88 μm , [N III] 57 μm and [N II] 122 μm lines originate from the foreground M42 H II region which is excited by the θ^1 Ori OB stars, known as ‘The Trapezium’ (see Figure 1); these lines provide an important tool for probing physical conditions and elemental abundances in the ionised gas (Simpson et al. 1986, Rubin et al. 1994).

4.1.2 Electron densities from the [O III] lines

The intensity ratio of the [O III] 52 μm and 88 μm lines provides an electron density diagnostic. The line ratio has almost no dependence on electron temperature because of the very low excitation energies of the transitions. The measured line fluxes give an 88.4 μm /51.8 μm flux ratio of $\sim 0.41 \pm 0.01$. Adopting the same atomic parameters as Liu et al. (2001), we obtain an electron density $N_e(\text{O III}) = 830 \pm_{140}^{200} \text{ cm}^{-3}$ calculated for $T_e = 8000 \text{ K}$.

Another important electron density indicator is the [S III] 33.5/18.7 μm ratio.

Table 4: Line measurements obtained from L03 and L04 high resolution observations towards the Orion KL region. Line fitting measurements were performed using a Lorentzian function. Quoted errors are based on goodness of fit estimations. Note that ⁽¹⁾ corresponds to a tentative detection with flux below 3σ ; ⁽²⁾ are blended lines and ⁽³⁾ are lines detected in the lower resolution L01 spectrum where no velocity peak information is given.

Species	Transition	Rest Wavelength (μm)	Flux absorption (10^{-17}W cm^{-2})	Flux emission (10^{-17}W cm^{-2})	Peak absorption (km s^{-1})	Peak emission (km s^{-1})
p-H ₂ O	5 ₄₂ - 4 ₃₁	44.195	0.48 ± 0.091	0.39 ± 0.20	-28.9 ± 5.5	53.6 ± 27.4
o-H ₂ O	5 ₂₃ - 4 ₁₄	45.111	1.11 ± 0.016	0.39 ± 0.091	-22.2 ± 2.1	39.7 ± 9.2
p-H ₂ O	3 ₃₁ - 2 ₀₂	46.484	1.05 ± 0.12		-10.6 ± 2.1	
p-H ₂ O	10 ₁₉ - 9 ₂₈	47.039	0.19 ± 0.041	0.49 ± 0.19	-3.1 ± 1.1	23.6 ± 9.1
o-H ₂ O	5 ₃₂ - 4 ₂₃	47.972	1.13 ± 0.14	0.55 ± 0.21	-16.3 ± 2.1	38.9 ± 14.8
OH	² Π _{1/2} - ² Π _{3/2} J=5/2 ⁻ - 5/2 ⁺	48.704	1.09 ± 0.13		-12.4 ± 1.4	
OH	² Π _{1/2} - ² Π _{3/2} J=5/2 ⁺ - 5/2 ⁻	48.817	1.34 ± 0.14		-22.8 ± 2.8	
p-H ₂ O	4 ₄₀ - 3 ₃₁	49.281	0.71 ± 0.13		-9.2 ± 1.6	
o-H ₂ O	4 ₄₁ - 3 ₃₀	49.336	1.82 ± 0.26	0.63 ± 0.14	-17.1 ± 2.4	48.1 ± 10.6
o-H ₂ O	6 ₃₄ - 5 ₂₃	49.390		0.99 ± 0.21		44.1 ± 9.3
p-H ₂ O	9 ₂₈ - 8 ₁₇	50.634		0.19 ± 0.02		35.4 ± 3.7
CO ⁽¹⁾	5 ₂ - 5 ₁	50.887		0.71 ± 0.23		1.1 ± 0.4
[OIII]	³ P ₂ - ³ P ₁	51.815		37.1 ± 0.50		7.2 ± 0.1
p-H ₂ O	5 ₃₃ - 4 ₂₂	53.137	0.24 ± 0.04	0.41 ± 0.03	-32.1 ± 5.4	36.5 ± 2.7
OH	² Π _{1/2} - ² Π _{3/2} J= 3/2 ⁺ - 3/2 ⁻	53.261	2.55 ± 0.32	1.10 ± 0.62	-20.7 ± 2.5	14.5 ± 8.1
OH	² Π _{1/2} - ² Π _{3/2} J= 3/2 ⁻ - 3/2 ⁺	53.351	2.45 ± 0.26	0.26 ± 0.13	-14.2 ± 1.5	45.1 ± 19.9
p-H ₂ O	4 ₃₁ - 3 ₂₂	56.324	1.09 ± 0.11	0.59 ± 0.25	-5.1 ± 0.5	44.9 ± 18.9
[NIII]	² P _{3/2} - ² P _{1/2}	57.329		5.97 ± 0.12		2.9 ± 0.1
p-H ₂ O	4 ₂₂ - 3 ₁₃	57.636	2.15 ^a ± 0.24	0.52 ± 0.19	-15.5 ± 1.7	48.9 ± 17.8
CO	4 ₅ - 4 ₄	58.547		0.12 ± 0.037		6.7 ± 2.1
o-H ₂ O	4 ₃₂ - 3 ₂₁	58.698	1.57 ± 0.13	1.80 ± 0.14	-29.9 ± 2.5	37.3 ± 2.9
HDO	3 ₃₀ - 2 ₁₁	59.928		0.15 ± 0.013		37.5 ± 3.2
p-H ₂ O	4 ₃₁ - 4 ₀₄	61.808		0.52 ± 0.02		43.5 ± 1.7
HDO	10 ₆₅ - 10 ₅₆	62.231		0.02 ± 0.006		4.5 ± 1.3
[OI]	³ P ₁ - ³ P ₂	63.184		65.33 ± 0.54		14.6 ± 0.1
p-H ₂ O	8 ₁₈ - 7 ₀₇	63.322		0.30 ± 0.12		30.3 ± 12.1
o-H ₂ O	8 ₀₈ - 7 ₁₇	63.457		0.27 ± 0.045		41.5 ± 6.9
OH	² Π _{3/2} J= 9/2 ⁻ - 7/2 ⁺	65.132	0.44 ± 0.091	0.84 ± 0.12	-22.9 ± 4.7	29.6 ± 4.2
o-H ₂ O	6 ₂₅ - 5 ₁₄	65.166		1.09 ± 0.13		26.4 ± 3.1
OH	² Π _{3/2} J= 9/2 ⁺ - 7/2 ⁻	65.279	0.39 ± 0.10	0.59 ± 0.20	-15.6 ± 3.9	34.9 ± 11.8
o-H ₂ O	7 ₁₆ - 6 ₂₅	66.092		0.78 ± 0.16		30.3 ± 6.2
o-H ₂ O	3 ₃₀ - 2 ₂₁	66.437	1.51 ± 0.18	1.39 ± 0.28	-22.2 ± 2.6	40.5 ± 8.1
p-H ₂ O	3 ₃₁ - 2 ₂₀	67.089	1.40 ± 0.21	1.07 ± 0.20	-12.7 ± 1.9	42.5 ± 7.9
H ₂ ¹⁸ O	3 ₃₀ - 2 ₂₁	67.191	0.19 ± 0.031		-12.9 ± 2.1	
o-H ₂ O ⁽¹⁾	3 ₃₀ - 3 ₀₃	67.269	0.33 ± 0.11	0.64 ± 0.11	-22.5 ± 7.5	32.5 ± 5.6
CO	3 ₉ - 3 ₈	67.336		0.48 ± 0.14		12.4 ± 3.6
CO	3 ₈ - 3 ₇	69.074		0.45 ± 0.14		15.5 ± 4.8
CO	3 ₇ - 3 ₆	70.907		0.70 ± 0.061		10.1 ± 0.9
p-H ₂ O	5 ₂₄ - 4 ₁₃	71.066	0.15 ± 0.039	0.89 ± 0.059	-22.5 ± 5.8	28.5 ± 1.8
OH	² Π _{1/2} J= 7/2 ⁻ - 5/2 ⁺	71.171		0.33 ± 0.049		28.2 ± 4.2
OH	² Π _{1/2} J= 7/2 ⁺ - 5/2 ⁻	71.218		0.78 ± 0.12		27.9 ± 4.3
p-H ₂ O	7 ₁₇ - 6 ₀₆	71.539		1.39 ± 0.13		22.3 ± 2.1
o-H ₂ O	7 ₀₇ - 6 ₁₆	71.946		1.42 ± 0.28		26.7 ± 5.2
CO	3 ₆ - 3 ₅	72.843		0.62 ± 0.13		1.6 ± 0.3
HDO ⁽¹⁾	9 ₆₃ - 10 ₄₆	74.792		0.07 ± 0.02		19.5 ± 5.6
CO	3 ₅ - 3 ₄	74.890		3.46 ± 0.40		0.1 ± 0.01
o-H ₂ O	3 ₂₁ - 2 ₁₂	75.380	0.88 ± 0.25	5.67 ± 0.21	-31.5 ± 8.9	28.5 ± 1.1
o-H ₂ O	5 ₅₁ - 5 ₄₂	75.779		0.32 ± 0.04		19.2 ± 2.4
H ₂ ¹⁸ O	3 ₂₁ - 2 ₁₂	75.868	0.08 ± 0.01		-10.1 ± 0.6	
o-H ₂ O	5 ₅₀ - 5 ₄₁	75.908		0.27 ± 0.01		20.1 ± 0.7
CO	3 ₄ - 3 ₃	77.059		0.60 ± 0.09		4.9 ± 0.7
o-H ₂ O	4 ₂₃ - 3 ₁₂	78.741		6.18 ± 0.17		26.9 ± 0.7
p-H ₂ O	6 ₁₅ - 5 ₂₄	78.928		0.43 ± 0.11		16.5 ± 4.2
OH	² Π _{3/2} J= 1/2 ⁻ - 3/2 ⁺	79.118		3.89 ± 0.16		16.4 ± 0.7
OH	² Π _{3/2} J= 1/2 ⁺ - 3/2 ⁻	79.182		3.73 ± 0.38		19.1 ± 1.9
CO	3 ₃ - 3 ₂	79.359		2.32 ± 0.20		3.7 ± 0.3
CO	3 ₂ - 3 ₁	81.806		1.52 ± 0.09		10.8 ± 0.6
o-H ₂ O	6 ₁₆ - 5 ₀₅	82.030		2.78 ± 0.13		22.4 ± 1.1
o-H ₂ O	8 ₃₆ - 8 ₂₇	82.974		0.27 ± 0.06		15.1 ± 3.2
p-H ₂ O	6 ₀₆ - 5 ₁₅	83.283		1.29 ± 0.08		31.1 ± 1.8
OH	² Π _{3/2} J= 7/2 ⁺ - 5/2 ⁻	84.420		1.72 ± 0.13		30.8 ± 2.3
o-H ₂ O ⁽¹⁾	11 ₄₈ - 10 ₅₅	84.514		0.15 ± 0.10		2.1 ± 1.4
OH	² Π _{3/2} J= 7/2 ⁻ - 5/2 ⁺	84.597	1.13 ± 0.38	1.34 ± 0.26	-21.4 ± 7.9	36.2 ± 7.1
o-H ₂ O ⁽²⁾	7 ₁₆ - 7 ₀₇	84.766		0.47 ± 0.05		19.2 ± 1.9
H ₂ ¹⁷ O ^(1,2)	7 ₁₆ - 7 ₀₇	84.778				
CO	3 ₀ - 2 ₉	87.190		1.58 ± 0.11		2.8 ± 0.2
[OIII]	³ P ₁ - ³ P ₀	88.356		13.2 ± 0.29		9.8 ± 0.1
o-H ₂ O	3 ₂₂ - 2 ₁₁	89.988		2.17 ± 0.17		29.1 ± 2.3
CO	2 ₉ - 2 ₈	90.163		1.58 ± 0.14		5.1 ± 0.4

⁽¹⁾ Tentative detections ⁽²⁾ Blended lines ⁽³⁾ L01 detection

Table 4 – Continued

Species	Transition	Rest Wavelength (μm)	Flux absorption (10^{-17}W cm^{-2})	Flux emission (10^{-17}W cm^{-2})	Peak absorption (km s^{-1})	Peak emission (km s^{-1})
p-H ₂ O	11 ₅₇ – 10 ₆₄	90.643		0.16 \pm 0.03		42.5 \pm 8.0
o-H ₂ O	6 ₄₃ – 6 ₃₄	92.811		0.49 \pm 0.06		8.9 \pm 1.1
CO	28 – 27	93.349		1.89 \pm 0.11		10.8 \pm 0.6
o-H ₂ O	7 ₃₅ – 7 ₂₆	93.379		0.36 \pm 0.05		20.5 \pm 2.9
p-H ₂ O	5 ₄₂ – 5 ₃₃	94.206		0.62 \pm 0.02		14.6 \pm 0.5
o-H ₂ O	6 ₂₅ – 6 ₁₆	94.643		0.52 \pm 0.06		22.7 \pm 0.3
o-H ₂ O	4 ₄₁ – 4 ₃₂	94.703		0.72 \pm 0.06		27.1 \pm 2.2
p-H ₂ O	5 ₁₅ – 4 ₀₄	95.626		1.42 \pm 0.10		27.4 \pm 1.3
p-H ₂ O	4 ₄₁ – 4 ₃₂	95.883		0.67 \pm 0.06		29.2 \pm 2.7
OH	$^2\Pi_{3/2} - ^2\Pi_{1/2}$ J= 3/2 ⁺ – 5/2 [–]	96.314		0.88 \pm 0.05		10.5 \pm 0.6
OH	$^2\Pi_{3/2} - ^2\Pi_{1/2}$ J= 3/2 [–] – 5/2 ⁺	96.368		0.74 \pm 0.03		13.4 \pm 0.6
CO	27 – 26	96.773		3.82 \pm 0.11		9.2 \pm 0.3
OH	$^2\Pi_{1/2}$ J= 5/2 [–] – 3/2 ⁺	98.725		3.61 \pm 0.33		38.8 \pm 3.5
OH ⁽²⁾	$^2\Pi_{1/2}$ J= 5/2 ⁺ – 3/2 [–]	98.737				15.7 \pm 3.5
o-H ₂ O	5 ₀₅ – 4 ₁₄	99.492		5.61 \pm 0.12		22.2 \pm 0.5
H ₂ ¹⁸ O ⁽¹⁾	5 ₀₅ – 4 ₁₄	99.784		0.03 \pm 0.01		24.6 \pm 0.8
CO	26 – 25	100.461		3.44 \pm 0.06		11.5 \pm 0.2
p-H ₃ O ⁺ ⁽¹⁾	2 ₁ [–] – 1 ₁ ⁺	100.577		0.03 \pm 0.01		
o-H ₃ O ⁺ ⁽¹⁾	2 ₀ [–] – 1 ₀ ⁺	100.869		0.09 \pm 0.05		
o-H ₂ O	5 ₁₄ – 4 ₂₃	100.913		3.05 \pm 0.17		21.1 \pm 1.2
p-H ₂ O	2 ₂₀ – 1 ₁₁	100.983		2.35 \pm 0.09		29.9 \pm 1.2
p-H ₂ O	6 ₂₄ – 5 ₃₃	101.210		0.19 \pm 0.04		14.8 \pm 2.9
H ₂ ¹⁸ O	2 ₂₀ – 1 ₁₁	102.008	0.22 \pm 0.03		-11.7 \pm 1.3	
p-H ₂ O	6 ₄₂ – 6 ₃₃	103.916		0.08 \pm 0.02		19.4 \pm 5.6
p-H ₂ O	6 ₁₅ – 6 ₀₆	103.939		0.11 \pm 0.02		18.5 \pm 3.7
o-H ₂ O	6 ₃₄ – 6 ₂₅	104.090		0.61 \pm 0.11		24.2 \pm 4.3
CO	25 – 24	104.445		3.67 \pm 0.10		8.32 \pm 0.2
o-H ₂ O	2 ₂₁ – 1 ₁₀	108.073		3.22 \pm 0.08		29.1 \pm 0.7
CO	24 – 23	108.763		3.28 \pm 0.12		9.7 \pm 0.4
H ₂ ¹⁸ O	2 ₂₁ – 1 ₁₀	109.350	0.08 \pm 0.02	0.18 \pm 0.013	-8.1 \pm 1.7	48.9 \pm 3.5
p-H ₂ O	5 ₂₄ – 5 ₁₅	111.626		0.43 \pm 0.03		26.7 \pm 1.7
o-H ₂ O	7 ₄₃ – 7 ₃₄	112.511		0.09 \pm 0.02		11.6 \pm 2.7
CO	23 – 22	113.458		4.82 \pm 0.15		10.4 \pm 6.3
o-H ₂ O	4 ₁₄ – 3 ₀₃	113.537		5.10 \pm 0.13		22.6 \pm 0.6
p-H ₂ O	5 ₃₃ – 5 ₂₄	113.944		1.38 \pm 0.06		27.6 \pm 1.3
H ₂ ¹⁸ O	4 ₁₄ – 3 ₀₃	114.297		0.16 \pm 0.01		44.6 \pm 1.7
OH	$^2\Pi_{3/2} - ^2\Pi_{1/2}$ J= 7/2 [–] – 5/2 ⁺	115.153		0.18 \pm 0.01		20.2 \pm 1.6
CO	22 – 21	118.581		6.58 \pm 0.09		12.5 \pm 0.2
OH	$^2\Pi_{3/2}$ J= 5/2 [–] – 3/2 ⁺	119.234	0.39 \pm 0.07	1.76 \pm 0.17	-45.5 \pm 8.4	33.9 \pm 3.3
OH	$^2\Pi_{3/2}$ J= 5/2 ⁺ – 3/2 [–]	119.442		2.42 \pm 0.15		35.5 \pm 2.2
¹⁸ OH ⁽¹⁾	$^2\Pi_{3/2}$ J= 5/2 ⁺ – 3/2 [–]	119.966	0.11 \pm 0.04	0.10 \pm 0.025	-25.8 \pm 9.1	51.4 \pm 12.8
¹⁸ OH ⁽¹⁾	$^2\Pi_{3/2}$ J= 5/2 [–] – 3/2 ⁺	120.172	0.03 \pm 0.01	0.031 \pm 0.005	-5.1 \pm 0.9	28.9 \pm 4.6
o-H ₂ O	4 ₃₂ – 4 ₂₃	121.719		2.28 \pm 0.13		28.1 \pm 1.6
[NII] ⁽¹⁾	$^3P_1 - ^3P_2$	121.890		0.93 \pm 0.47		
CO	21 – 20	124.193		7.89 \pm 0.58		15.0 \pm 1.1
o-NH ₃	4 ₃ [–] – 3 ₃ ⁺	124.647		0.08 \pm 0.01		40.8 \pm 2.3
p-NH ₃ ⁽¹⁾	4 ₂ [–] – 3 ₂ ⁺	124.796		0.03 \pm 0.01		11.5 \pm 0.5
o-NH ₃	4 ₀ [–] – 3 ₀ ⁺	124.913		0.05 \pm 0.01		8.6 \pm 0.6
HDO	5 ₃₃ – 5 ₂₄	124.954		0.02 \pm 0.004		9.1 \pm 1.9
p-H ₂ O	4 ₀₄ – 3 ₁₃	125.354		2.25 \pm 0.09		25.5 \pm 1.1
p-H ₂ O	3 ₃₁ – 3 ₂₂	126.713		0.62 \pm 0.08		30.5 \pm 4.1
o-H ₂ O	7 ₂₅ – 7 ₁₆	127.882		0.24 \pm 0.03		26.4 \pm 3.1
¹³ CO ⁽¹⁾	21 – 20	129.891		0.02 \pm 0.01		10.3 \pm 3.9
CO	20 – 19	130.369		6.19 \pm 0.22		16.1 \pm 0.6
o-H ₂ O	5 ₁₄ – 5 ₀₅	134.935		0.86 \pm 0.05		25.4 \pm 1.6
HDO	4 ₃₁ – 4 ₂₂	135.425		0.08 \pm 0.02		17.5 \pm 4.1
o-H ₂ O	3 ₃₀ – 3 ₂₁	136.494		0.71 \pm 0.05		30.9 \pm 2.3
CO	19 – 18	137.196		5.22 \pm 0.05		18.4 \pm 0.2
p-H ₂ O	3 ₁₃ – 2 ₀₂	138.527		2.67 \pm 0.03		26.4 \pm 0.3
p-H ₂ O	4 ₁₃ – 3 ₂₂	144.517		1.15 \pm 0.07		18.4 \pm 0.2
CO	18 – 17	144.784		3.98 \pm 0.26		15.5 \pm 1.1
[OI]	$^3P_0 - ^3P_1$	145.525		1.17 \pm 0.19		28.5 \pm 4.6
p-H ₂ O	4 ₃₁ – 4 ₂₂	146.919		1.14 \pm 0.06		22.1 \pm 1.1
CO	17 – 16	153.267		8.66 \pm 0.13		14.6 \pm 0.2
p-H ₂ O	3 ₂₂ – 3 ₁₃	156.193		1.23 \pm 0.08		32.5 \pm 2.2
o-H ₂ O	5 ₂₃ – 4 ₃₂	156.266		1.09 \pm 0.22		16.7 \pm 3.4
[CII]	$^2P_{3/2} - ^2P_{1/2}$	157.741		2.23 \pm 0.06		14.9 \pm 0.4
p-H ₂ O	5 ₃₂ – 5 ₂₃	160.504		0.45 \pm 0.06		24.9 \pm 3.2
CO	16 – 15	162.812		9.48 \pm 0.26		12.7 \pm 0.4

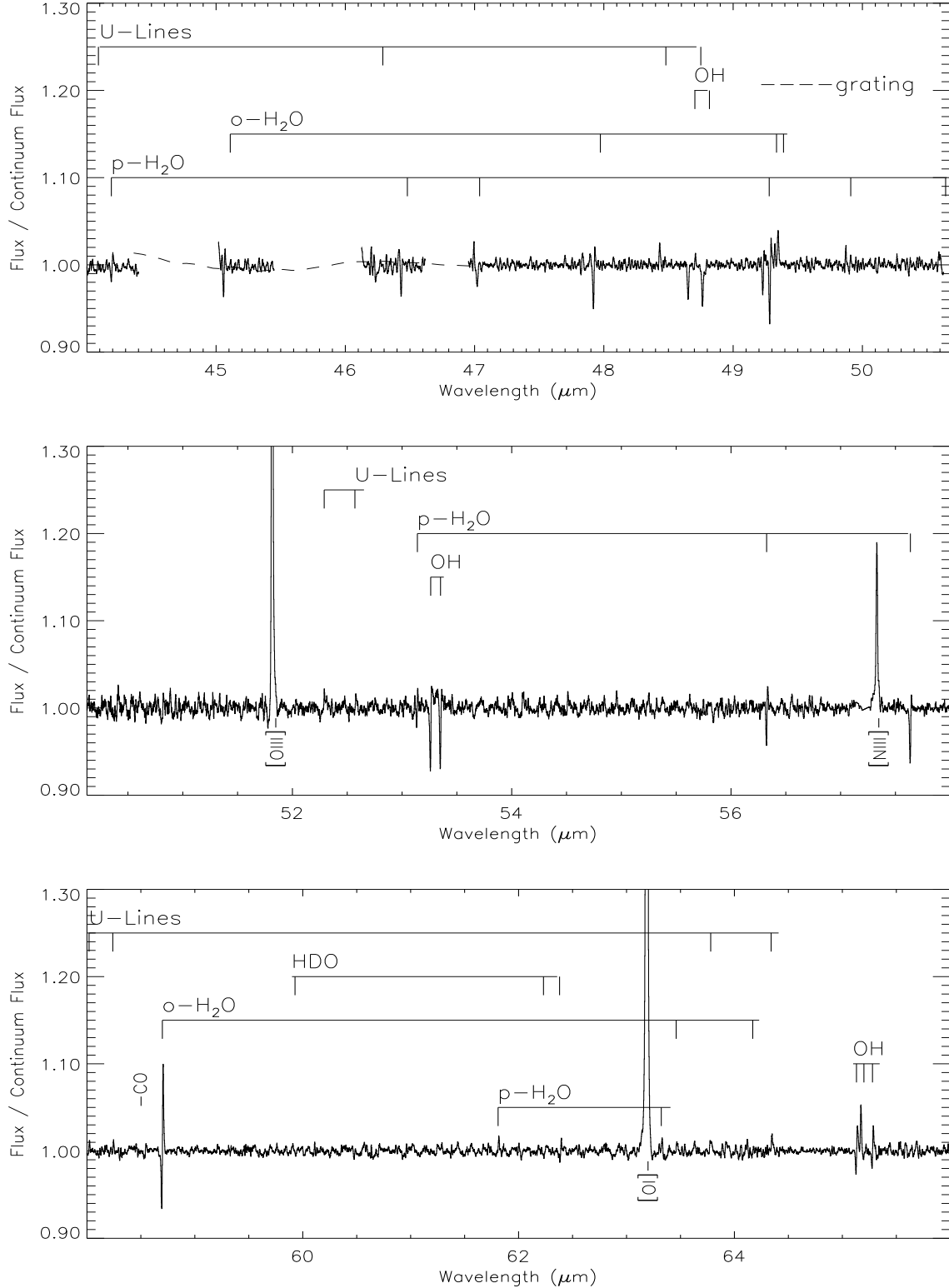
⁽¹⁾ Tentative detections ⁽²⁾ Blended lines ⁽³⁾ L01 detection

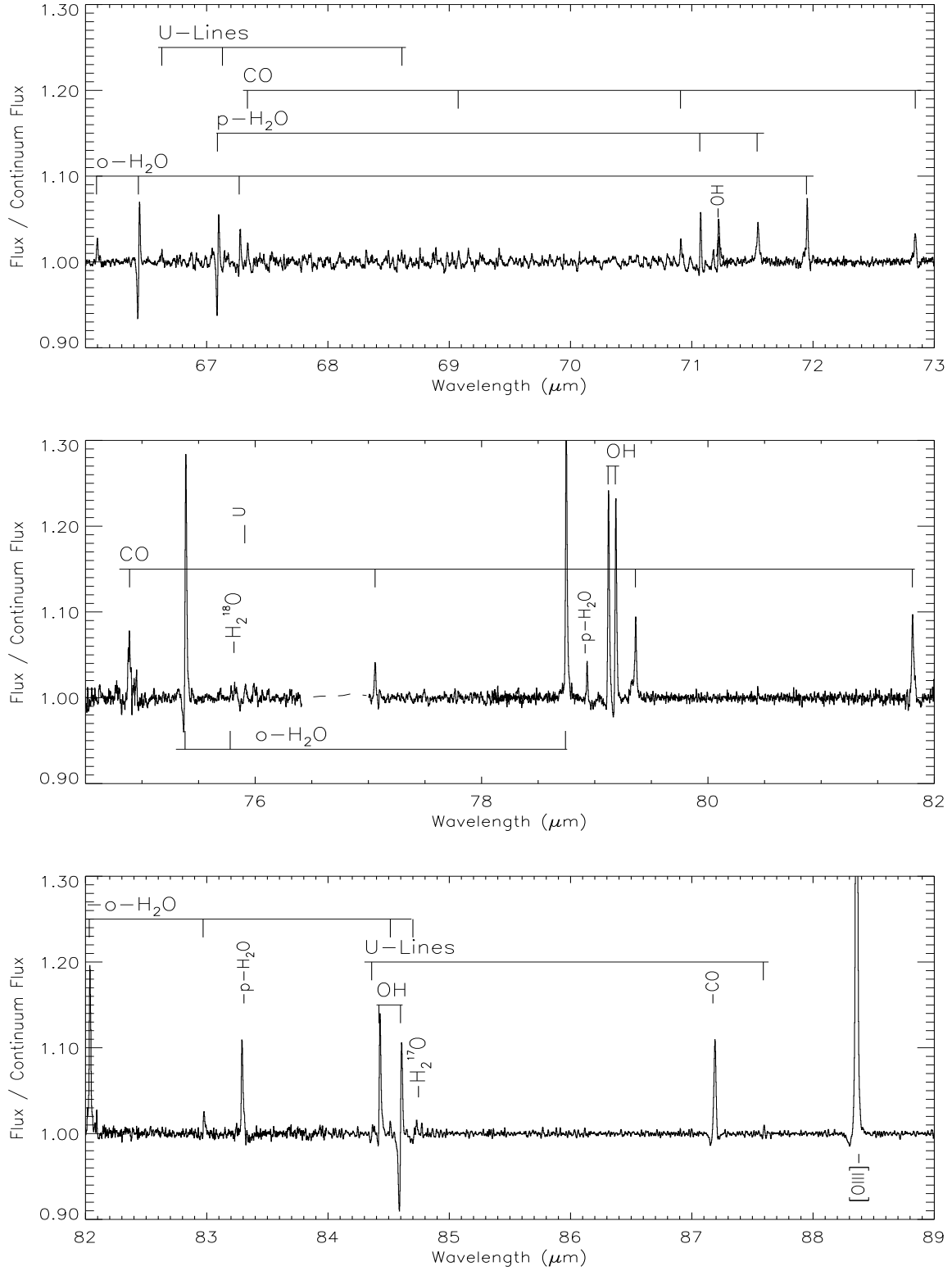
Table 4 – Continued

Species	Transition	Rest Wavelength (μm)	Flux absorption ($10^{-17} \text{W cm}^{-2}$)	Flux emission ($10^{-17} \text{W cm}^{-2}$)	Peak absorption (km s^{-1})	Peak emission (km s^{-1})
OH	$^2\Pi_{3/2} \text{ J}=3/2^+ - 1/2^-$	163.131		0.81 ± 0.19		17.4 ± 4.1
OH	$^2\Pi_{3/2} \text{ J}=3/2^- - 1/2^+$	163.397		1.66 ± 0.38		17.7 ± 4.1
p-NH ₃	$3_2^- - 2_2^+$	165.596		0.11 ± 0.02		14.4 ± 2.3
p-H ₂ O	$6_{33} - 6_{24}$	170.131		0.27 ± 0.01		43.5 ± 1.3
CO ⁽³⁾	$15 - 14$	173.631		9.80 ± 0.69		
H ₂ ¹⁸ O	$3_{03} - 2_{12}$	174.379		1.01 ± 0.06		3.2 ± 1.1
H ₂ ¹⁷ O ⁽¹⁾	$3_{03} - 2_{12}$	174.491		0.01 ± 0.004		4.8 ± 1.9
o-H ₂ O	$3_{03} - 2_{12}$	174.626		2.38 ± 0.19		20.1 ± 1.6
o-H ₂ O	$4_{32} - 5_{05}$	174.914		0.16 ± 0.01		23.5 ± 1.3
o-H ₂ O	$2_{12} - 1_{01}$	179.527		2.55 ± 0.31		23.8 ± 2.9
o-H ₂ O	$2_{21} - 2_{12}$	180.488		1.03 ± 0.11		23.8 ± 2.5
p-H ₃ O ⁺ ⁽²⁾	$1_1^- - 1_1^+$	181.054		0.05 ± 0.01		11.6 ± 0.3
H ₂ ¹⁸ O ⁽²⁾	$2_{21} - 1_{01}$	181.053				
CO ⁽³⁾ ^(2,3)	$14 - 13$	185.999		7.58 ± 0.22		
p-H ₂ O ^(2,3)	$4_{13} - 4_{04}$	187.110				

⁽¹⁾ Tentative detections ⁽²⁾ Blended lines ⁽³⁾ L01 detection

Figure 6. The complete Orion KL spectral survey obtained by the *ISO* LWS in Fabry-Pérot modes L03 and L04. The grating observation (L01 mode) is superimposed in regions where high resolution data are not available.



**Figure 6.** Continued

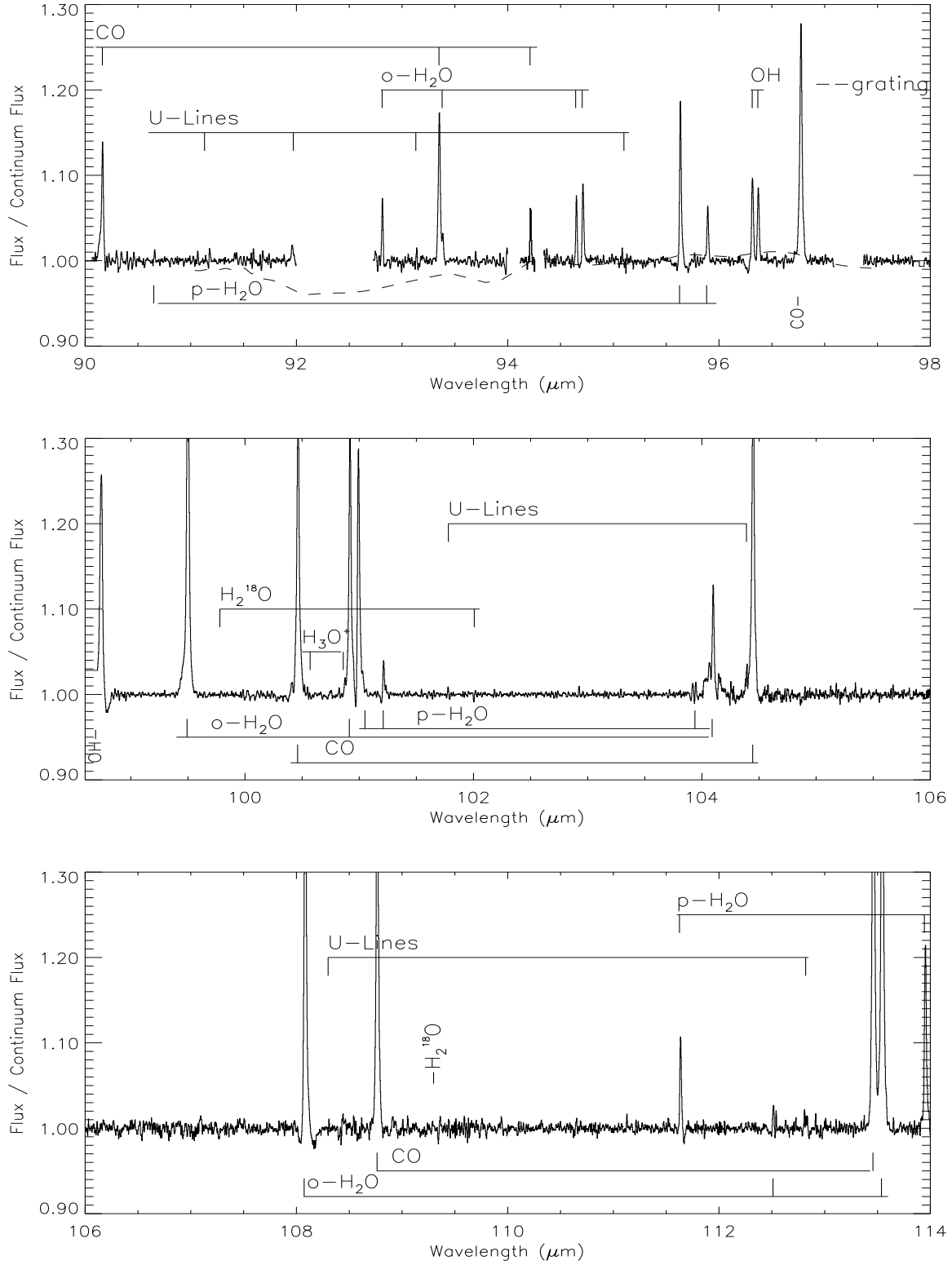


Figure 6. Continued

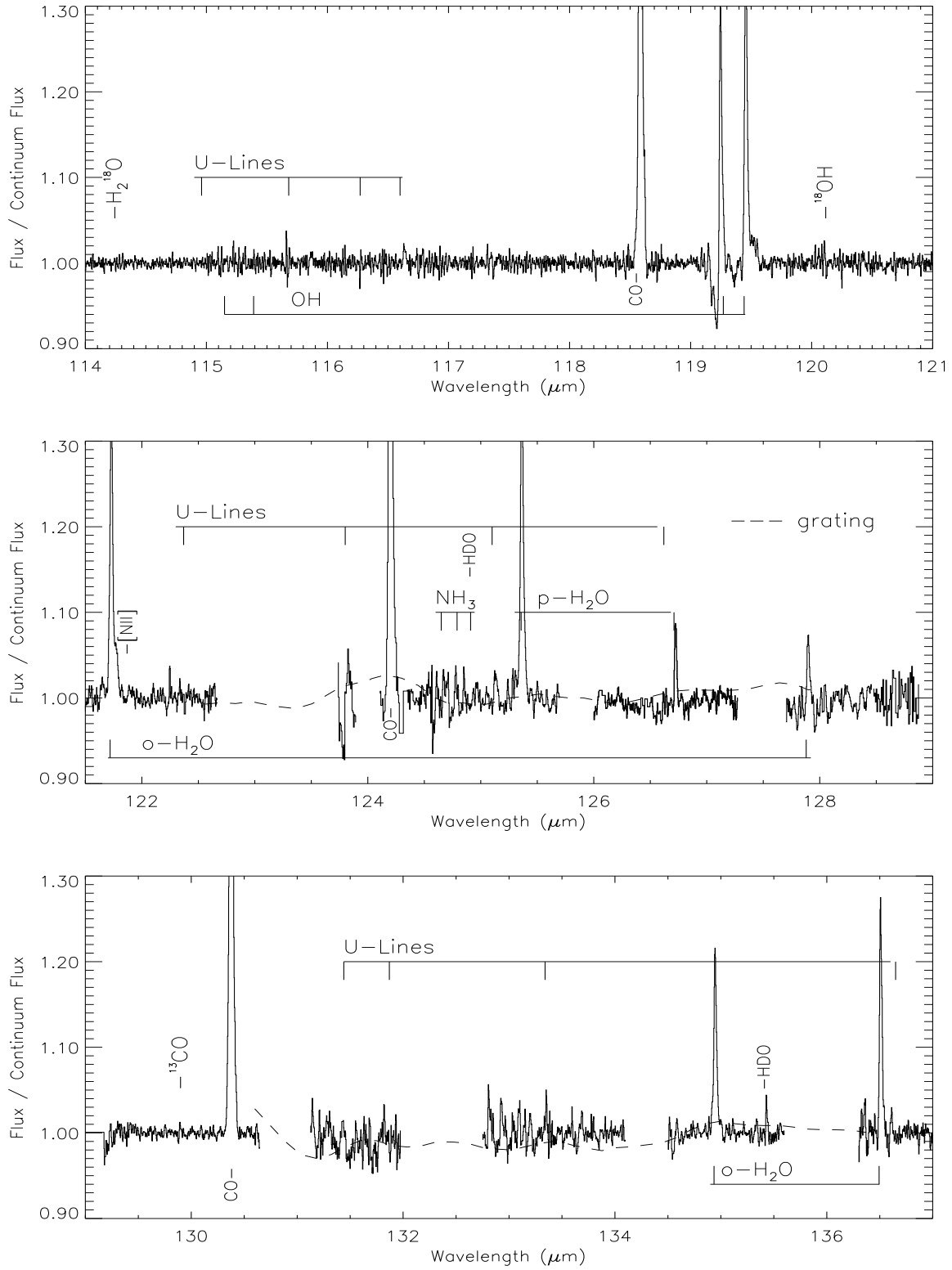


Figure 6. Continued

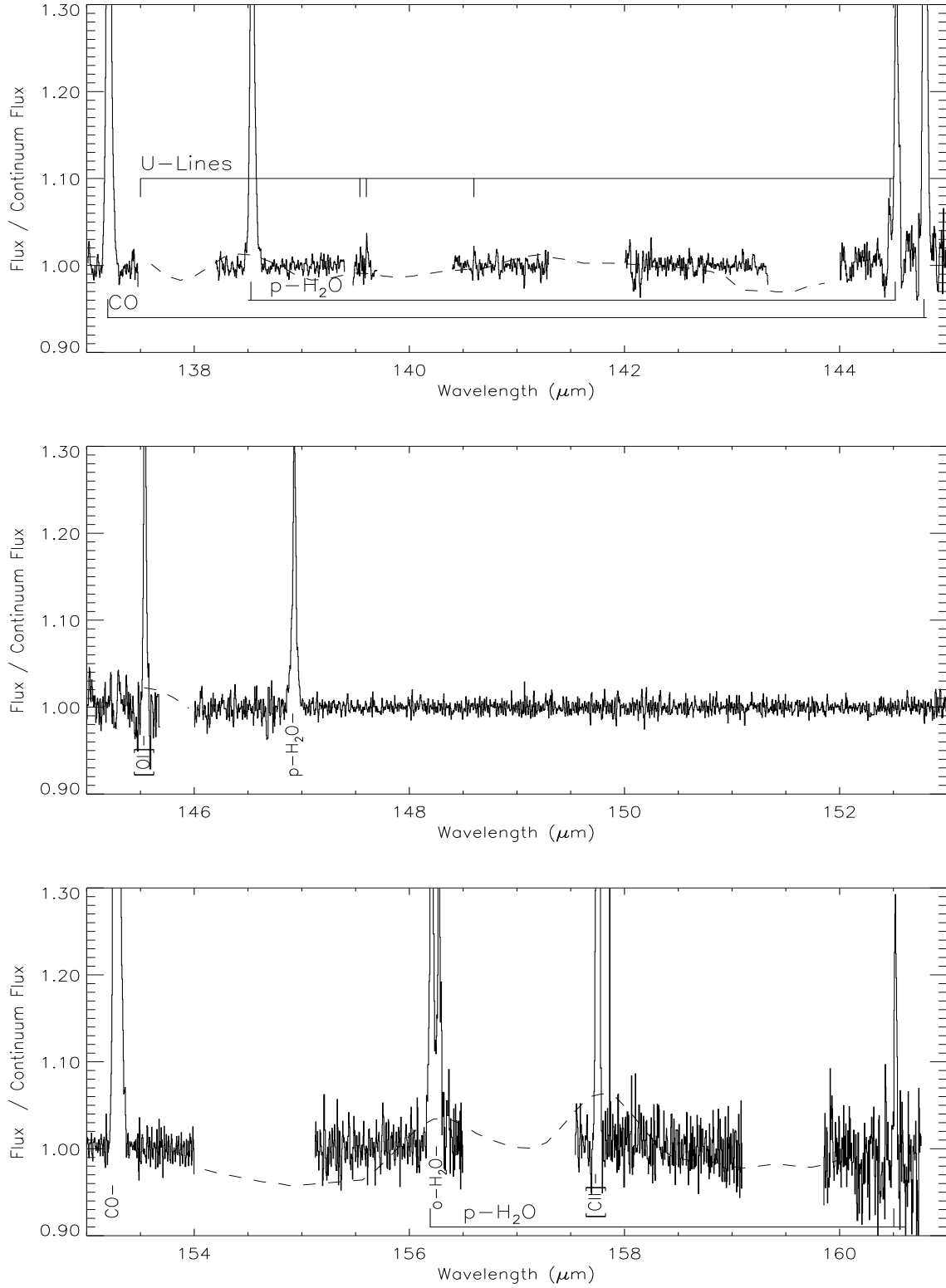


Figure 6. Continued

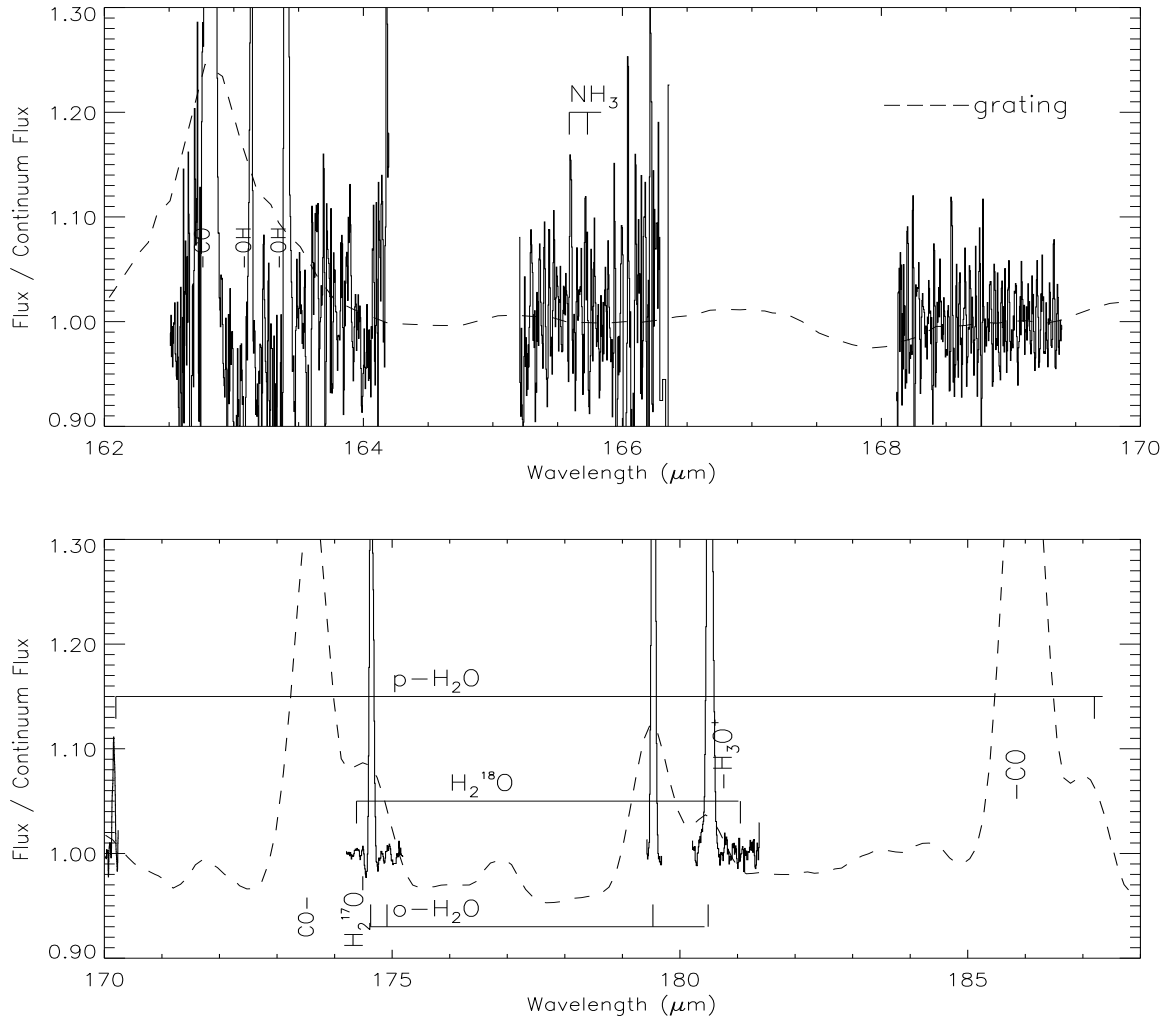


Figure 6. Continued. Note that features with no label on the L01 spectrum are non real features transferred by the calibration stage.

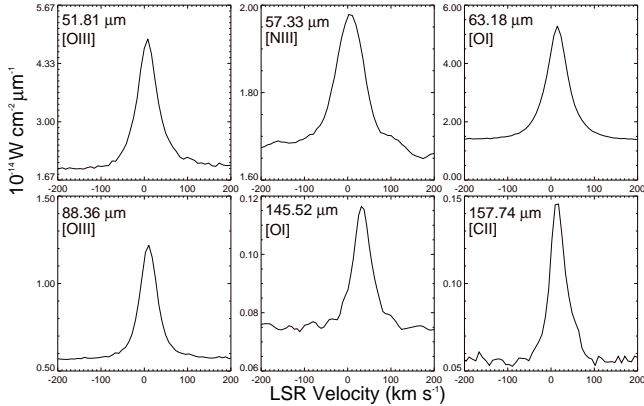


Figure 7. Transitions of [O III], [N III], [O I] and [C II] detected by the *ISO* LWS spectral survey towards Orion KL. Note that the LSR velocity of the line peaks (except for the [O I] line at 145.5 μm) is $\approx 10 \text{ km s}^{-1}$, in agreement with the velocity of the quiescent gas ($\approx 9 \text{ km s}^{-1}$).

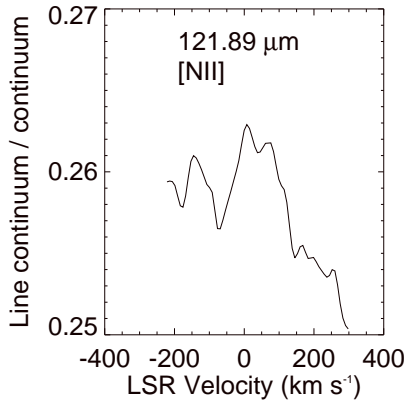


Figure 8. Tentative detection of the 122 μm line of [N II]. The broadness is due to hyperfine components in the transition as can be seen in the detection of the [N II] 122 μm line in Sgr B2 (Polehampton et al. 2006 in prep.)

These lines were detected by the Short Wavelength Spectrometer (SWS) towards IRc2 and the inferred [S III] 33.5/18.7 μm ratio was found to be ~ 0.55 (van Dishoeck et al. 1998). This ratio gives an $N_e(\text{S III})$ of $\approx 1950 \text{ cm}^{-3}$, which exceeds $N_e(\text{O III})$ by a factor of two, probably due to the higher critical densities of the [S III] lines.

4.2 [O I] and [C II]

The [C II] 157.7 μm and [O I] 63.2, 145.5 μm lines are important coolants in photodissociation regions (PDRs), whose heating is thought to be dominated by energetic photoelectrons ejected from dust grains following FUV photon absorption (Tielens & Hollenbach 1985). As important coolants, these lines can also originate in shocks driven by jets and outflows from young stellar objects (Hollenbach & McKee 1989).

The Orion nebula is an H II region which is ionised by the Trapezium stars. The luminosity of the ionising stars is about $10^5 L_\odot$, located approximately 0.15 pc from the molecular cloud leading to an incident FUV flux of about $G \approx 10^5 G_0$ (Tielens & Hollenbach 1985). The fraction of the FUV flux converted into line emission in these transitions is generally of the order $10^{-2} - 10^{-3}$ (Tielens & Hollenbach 1985) and is a function of both the gas temperature and the electron density.

The [C II] 157.7 / [O I] 63.2 μm ratio in Orion KL inferred from our observations is 3.42×10^{-2} , in good agreement with Tielens & Hollenbach's predictions. The [O I] 63.2/145.5 μm ratio combined with the [O I] 63.2 μm / [C II] 157.7 μm flux ratio can also be used to derive the temperature and density of PDRs (Watson 1983). Using the PDR temperature density plane defined in Liu et al. 2001, we inferred a temperature of 300 K and a density of $\log N_H = 5.4 \text{ cm}^{-3}$. Considering this, it seems natural to postulate that the lines originate in the PDR region. However, Orion KL could also be an important shock region (Chernoff, Hollenbach & McKee 1982) and a potential major contribution to [O I] emission from dissociated shocked gas should be taken into account.

Table 6 lists the surface brightnesses measured with the 80'' LWS beam compared with those observed towards θ^1 Ori C (column 3) by the *KAO* with a $\approx 45''$ beam (Melnick, Gull, & Harwit 1979; Ellis & Werner 1985; Werner et al. 1984; Stacey, Smyers, Kurtz & Harwit 1983; Russell et al. 1980; Phillips & Huggins 1981). Column 5 lists predicted line surface brightnesses from the photodissociation model of Tielens et al. (1985) and column 6 lists the predicted line surface brightnesses from the dissociative shock model of Hollenbach & McKee (1989) (for $n_0 = 10^5 \text{ cm}^{-3}$ and $v = 30 - 80 \text{ km s}^{-1}$).

We found that although our [O I] 63.18 μm and [O I] 145.52 μm line intensities are in good agreement with the shock model prediction, the observed [C II] line intensity is much higher than predicted by shock models. A PDR model can reproduce the *ISO* LWS [O I] 63.2 μm and [C II] surface brightness levels within 35%, although over-predicting the LWS [O I] 145.5 μm emission by a factor of 2.7. We note, however, that for the smaller beam *KAO* observations the PDR model can match the observed surface brightness levels for all three lines.

4.3 Molecular species

4.3.1 Water lines

High velocity gas was first detected at the centre of the Orion-KL region as broad wings on 'thermal' molecular lines in the millimeter range and as high velocity maser features in the 22 GHz line of H_2O (Genzel et al. 1981). These high velocity motions may be caused by mass outflows from newly formed stars. Many theoretical studies of the Orion region (e.g. Draine & Roberge 1982; Chernoff et al. 1982; Neufeld & Melnick 1987) have concluded that the rich emission spectrum from thermally excited water vapour should play a significant role in cooling the gas.

In conditions where the temperature exceeds $\sim 400 \text{ K}$, OH

Table 5. Detected fine-structure lines

Species	Transition	Rest Wavelength (μm)	Flux (W cm^{-2})
[O III]	$^3\text{P}_0 - ^3\text{P}_1$	51.814	$(3.71 \pm 0.005) \times 10^{-16}$
[N III]	$^2\text{P}_{3/2} - ^2\text{P}_{1/2}$	57.329	$(5.97 \pm 0.12) \times 10^{-17}$
[O I]	$^3\text{P}_1 - ^3\text{P}_2$	63.184	$(6.53 \pm 0.05) \times 10^{-16}$
[O III]	$^3\text{P}_1 - ^3\text{P}_0$	88.356	$(1.52 \pm 0.03) \times 10^{-16}$
[N II]	$^3\text{P}_1 - ^3\text{P}_2$	121.889	$(9.3 \pm 4.7) \times 10^{-19}$
[O I]	$^3\text{P}_1 - ^3\text{P}_0$	145.525	$(1.17 \pm 0.19) \times 10^{-18}$
[C II]	$^2\text{P}_{3/2} - ^2\text{P}_{1/2}$	157.741	$(2.23 \pm 0.06) \times 10^{-19}$

Species	Wavelength (μm)	<i>KAO</i> at θ^1 Ori C ($\text{ergs cm}^{-2} \text{ s}^{-1} \text{ sr}^{-1}$)	<i>ISO</i> LWS BN/KL ($\text{ergs cm}^{-2} \text{ s}^{-1} \text{ sr}^{-1}$)	PDR model ($\text{ergs cm}^{-2} \text{ s}^{-1} \text{ sr}^{-1}$)	Shock model ($\text{ergs cm}^{-2} \text{ s}^{-1} \text{ sr}^{-1}$)
[O I]	63.18	$4\text{--}6 \times 10^{-2}$	5.5×10^{-2}	4.6×10^{-2}	6.0×10^{-2}
[O I]	145.52	$3\text{--}6 \times 10^{-3}$	1.3×10^{-3}	3.5×10^{-3}	1.2×10^{-3}
[C II]	157.74	$4\text{--}7 \times 10^{-3}$	2.5×10^{-3}	3.8×10^{-3}	$< 1 \times 10^{-4}$

Table 6. Comparison of the observed line intensities towards Orion KL with the PDR model calculations of Tielens et al. (1984) and the shock model of Hollenbach et al. (1989).

and H_2O are rapidly formed through the following reactions (Elitzur & Watson 1978):



At higher temperatures, OH is also formed via molecular oxygen destruction:



eventually being processed into water again by reaction (2). Consequently, OH and H_2O fractional abundances increase in shocks and so does the overall rate of reaction. Molecules and atoms behind a shock front act as cooling agents by emitting infrared and microwave photons. Collisions between molecules at high temperature populate the vibrational and rotational levels of the molecules. Following these reactions, rotational and vibrational water transitions are predicted to occur, providing a ubiquitous tracer of shock-heated gas.

The widespread nature of the water vapour around IRC2 has been probed with maps at 183 GHz (Cernicharo et al. 1990, 1994, Cernicharo & Crovisier, 2005), the first time that its abundance was estimated in the different large-scale components of Orion IRC2. Harwit et al. (1998) analysed 8 lines of water observed by LWS FP in L04 mode, concluding that these lines arise from a molecular cloud subjected to a magnetohydrodynamic C-type shock. From their modelling, they derived an $\text{H}_2\text{O}/\text{H}$ abundance of 5×10^{-4} . However, the interpretation of these lines in the $\approx 80''$ LWS beam and the determination of the water abundance in the different components of Orion remains a long standing problem. This is basically due to two main issues: the complexity of the different dynamical and chemical processes that take place within the region encompassed by the LWS beam, including outflows and several gas components, and the need for new H_2O collisional rates appropriate for the temperatures prevailing in shocks.

Water lines appear in the survey as resolved (typically 70

km s^{-1} FWHM) with a total of 70 detected lines. The line profiles range from predominantly P-Cygni at shorter wavelengths to predominantly pure emission at longer wavelengths (see Figure 9). Radial velocities appear to be centred at $\approx -15 \text{ km s}^{-1}$ in all absorption lines (shorter wavelengths) consistent with the results found in the SWS range (from $2 \mu\text{m}$ to $45 \mu\text{m}$, van Dishoeck et al. 1998; Wright et al. 2000). However, the pure emission lines of H_2O peak at around $\approx +30 \text{ km s}^{-1}$ (see Section 4.4), where the velocity of the quiescent gas is 9 km s^{-1} (Cohen et al. 2006). The same behaviour is found for OH lines, where this has been interpreted as evidence of an outflow at a velocity of $\geq 25 \pm 5 \text{ km s}^{-1}$ (see discussion in Section 4.3.3; also Goicoechea et al. 2006).

4.3.2 Water isotopes

Several transitions of the water isotopic variants H_2^{17}O , H_2^{18}O and HDO are detected in the survey (Figure 10 and Figure 11). The detection of isotopes is of special interest for abundance determinations and the interpretation of the spatial origin of the lines. These lines are excellent water tracers as they are more likely to be optically thin, so that they can be used to derive the water abundance via the adoption of a $[\text{H}_2^{16}\text{O}]/[\text{H}_2^{18}\text{O}]$ isotopic ratio.

The detections of H_2^{18}O at $67.19 \mu\text{m}$ and $102.01 \mu\text{m}$ are of particular interest (see Figure 10). These H_2^{18}O lines show a main absorption component that contrasts with the equivalent H_2^{16}O transitions at $66.43 \mu\text{m}$ and $100.98 \mu\text{m}$, which appear as a P-Cygni and an emission line, respectively. The fact that both lines peak at $\approx -10 \text{ km s}^{-1}$ LSR can be interpreted as indicating an origin in the main outflow.

The H_2^{18}O rotational diagram (Figure 12) leads to a column density of $N_{\text{col}} \approx 2.8 \times 10^{14} \text{ cm}^{-2}$ and $T_{\text{rot}} = 60 \text{ K}$. If we adopt $[\text{H}_2^{16}\text{O}]/[\text{H}_2^{18}\text{O}] = 500$ (Bergin et al. 1998), the estimated total H_2O column density is $\approx 1.5 \times 10^{17} \text{ cm}^{-2}$.

However, the interpretation of the exact spatial origin of the water lines is not straightforward and requires more

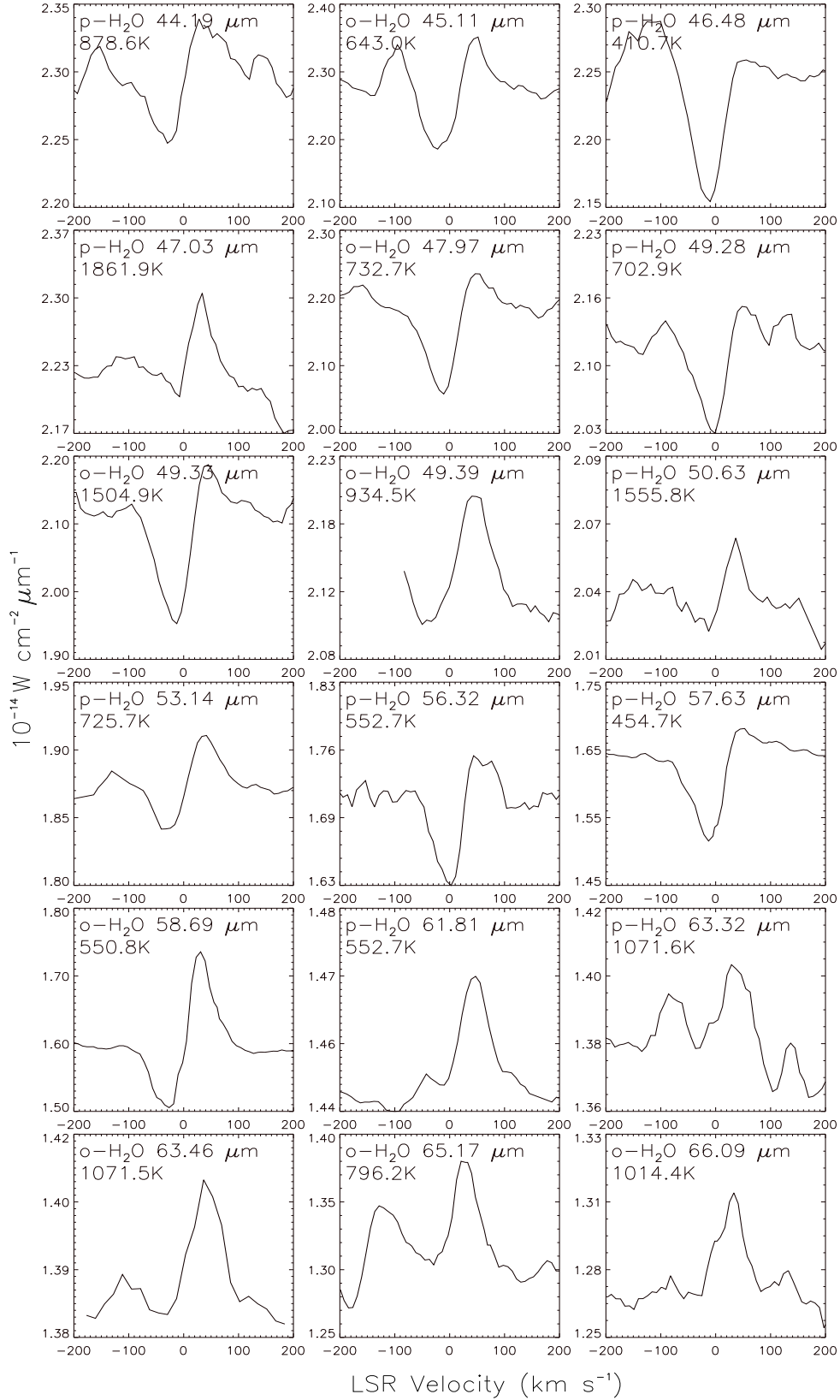
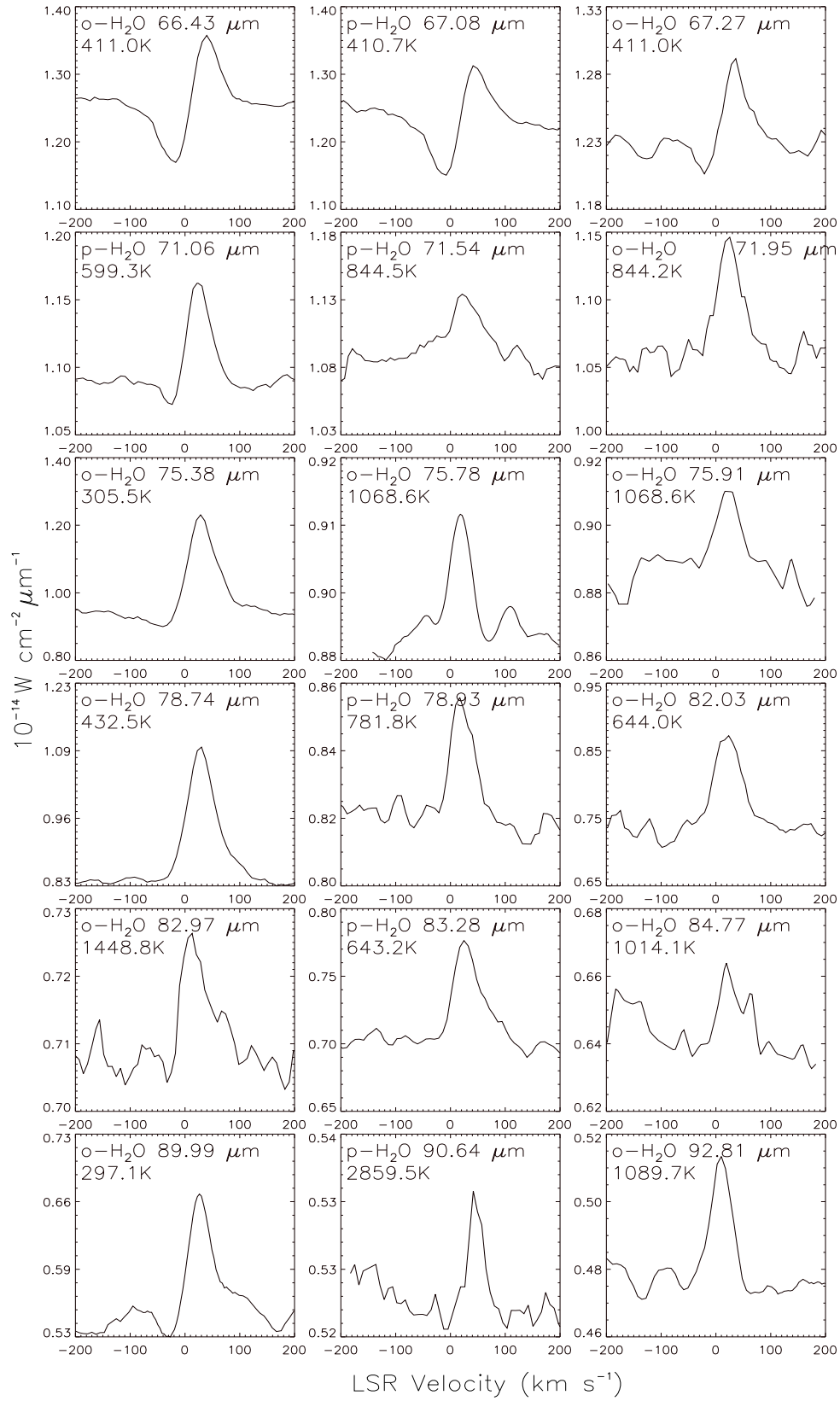


Figure 9. Water lines detected by the survey towards Orion KL

**Figure 9.** Continued

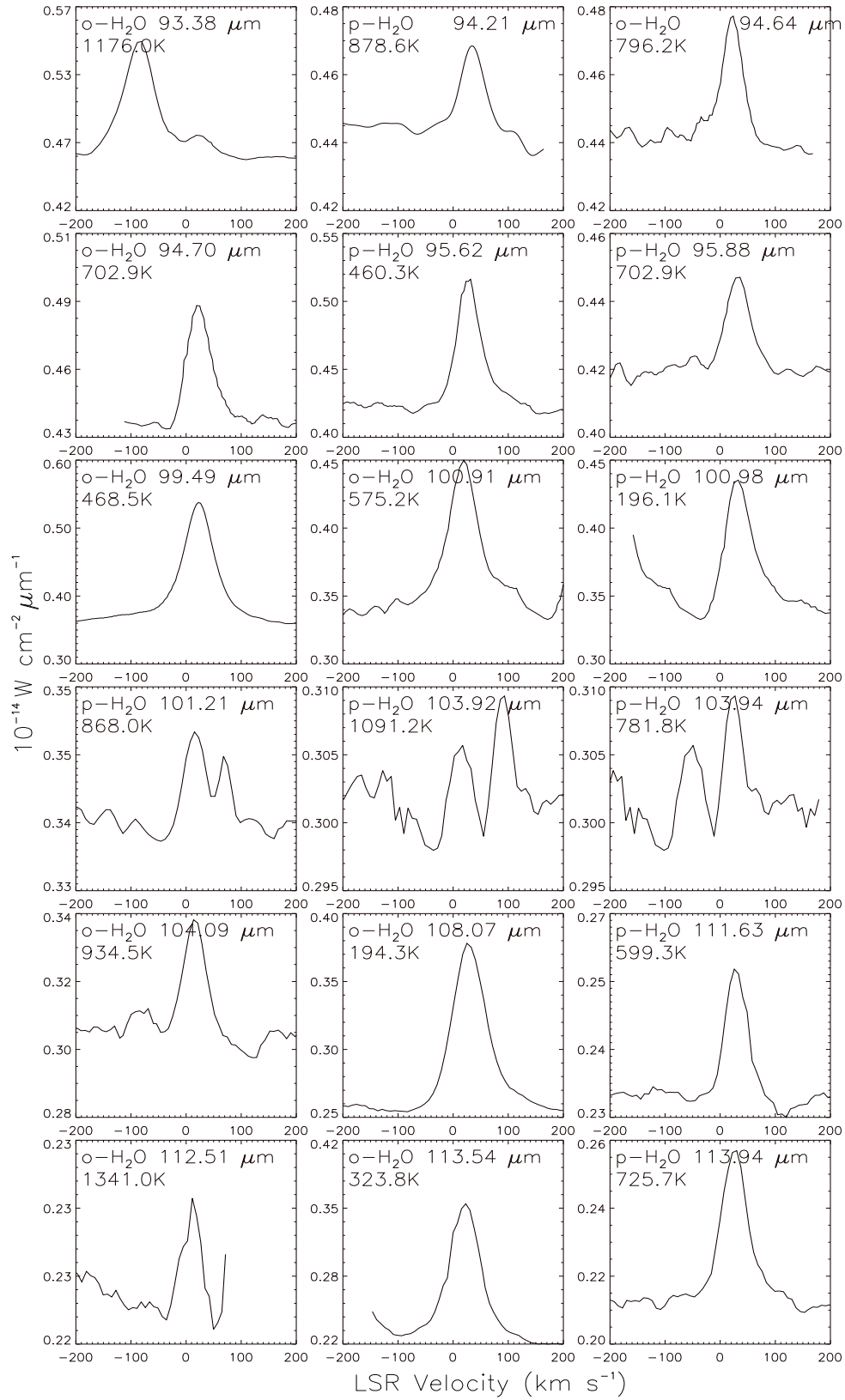
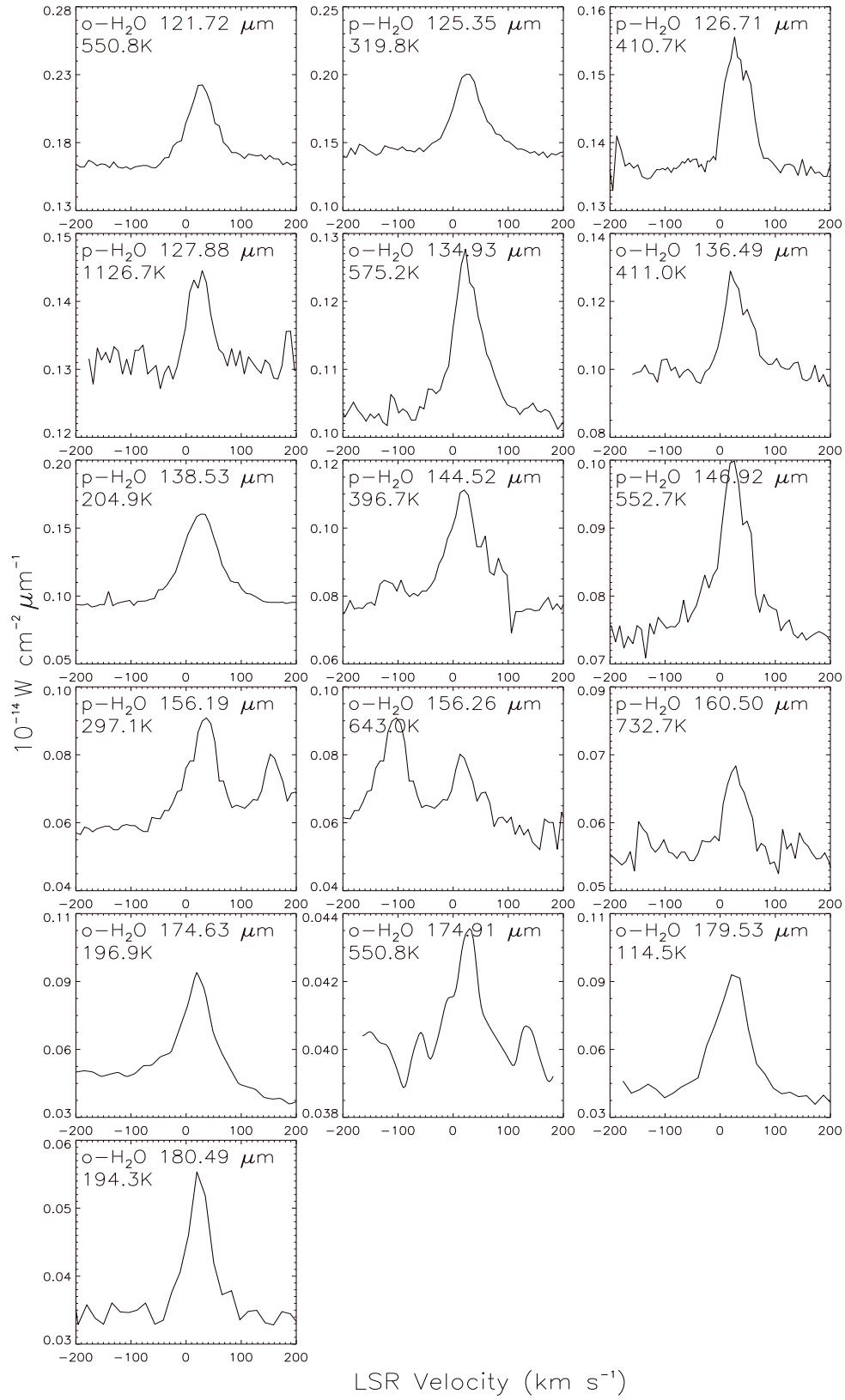


Figure 9. Continued

**Figure 9.** Continued

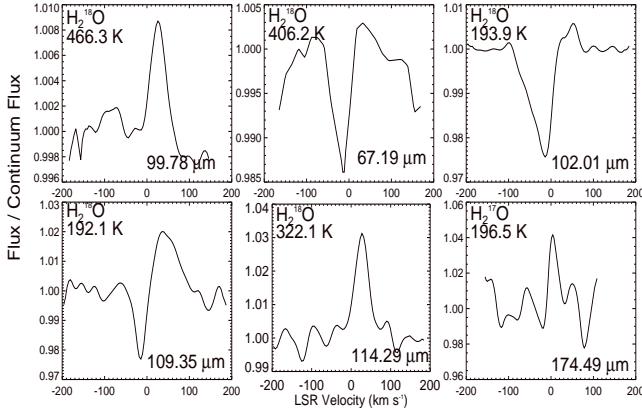


Figure 10. A selection of water isotope lines detected by the survey

sophisticated models. A detailed study of these lines will be published in future papers (Cernicharo et al. in preparation) and is beyond the scope of this work.

A total of 5 far-infrared HDO lines are tentatively identified for the first time towards Orion KL, from $3_{30} \rightarrow 2_{11}$ at 59.93 μm to $4_{31} \rightarrow 4_{22}$ at 135.42 μm (see Figure 11). The HDO rotational diagram gives a total column density of $N_{\text{col}} \approx 3 \times 10^{14} \text{ cm}^{-2}$. This value is significantly lower than that obtained from millimeter wave observations (Turner et al. 1975, Beckman et al. 1982, Moore et al. 1986). However, if the main HDO emission originated in the Hot Core, a low column density could be explained if the emission from the core is blocked by the intermediate-velocity gas. This hypothesis was previously pointed out by Pardo et al. (2001) in their analysis of the first detections of two submillimeter HDO lines from the KL region (transitions $2_{12} \rightarrow 1_{11}$ at 848.9 GHz and $1_{11} \rightarrow 0_{00}$ at 893.6 GHz), where the total HDO column density was estimated to be in the range $(4 - 6) \times 10^{16} \text{ cm}^{-2}$.

They concluded that the HDO transitions detected at above 800 GHz arise mainly from a very compact region (HPW 15'') in the Plateau. Our lower column density result ($\approx 10^{14} \text{ cm}^{-2}$) could therefore be explained if the compact HDO emission is diluted within the LWS beam. Special care has to be taken in the interpretation of tentative detections as the rotational diagram for these HDO lines could underestimate the total column density. More sophisticated models are needed to aid the interpretation.

4.3.3 OH Lines

Far-infrared line emission from excited OH rotational states was first detected toward the embedded star-forming region in Orion KL by Storey et al. (1981) using the KAO. In these early measurements, the ${}^2\Pi_{3/2} J=5/2 \rightarrow 3/2$ features at 119.23 μm and 119.44 μm were seen in emission. The fact that the excitation temperature above the ground state for $J_{\text{up}}=5/2$ is about 121 K and that the OH was observed $\approx 30''$ north of KL, led these authors to assume that the emission they detected came from the shocked gas region surrounding BN/KL.

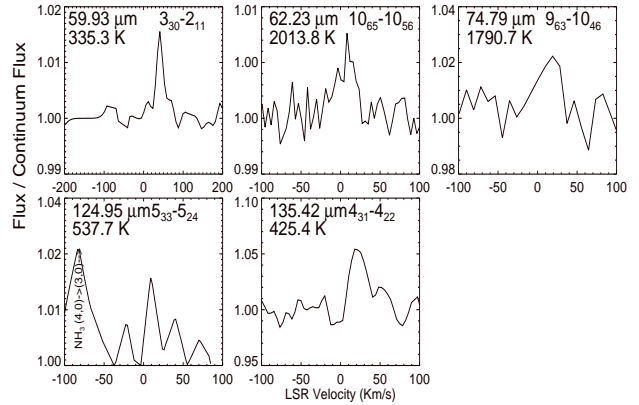


Figure 11. Tentative detections of five transitions of HDO observed towards Orion KL

Watson et al. (1985) reported KAO observations of the two lowest lying pure rotational transitions in the ${}^2\Pi_{3/2}$ electronic state of OH, at 119 μm and 84 μm . Melnick et al. (1990) modelled these detections, along with their own KAO detections of the ${}^2\Pi_{1/2} J=3/2 \rightarrow 1/2$ line at 163 μm , the ${}^2\Pi_{1/2} \rightarrow {}^2\Pi_{3/2} J=3/2^- \rightarrow 3/2^+$ line at 53 μm and the ${}^{18}\text{OH } {}^2\Pi_{3/2} J=5/2^+ \rightarrow 3/2^-$ line at 119.44 μm . They found that the best fit to the data required the presence of at least three components (see discussion below).

A total of 22 transitions of OH are detected by our survey, ranging from the ${}^2\Pi_{1/2} \rightarrow {}^2\Pi_{3/2} J=5/2^- \rightarrow 5/2^+$ transition at 48.7 μm to the ${}^2\Pi_{3/2} J=3/2^- \rightarrow 1/2^+$ transition at 163.4 μm . These transitions range up to upper energy levels of $\approx 618\text{K}$. Their line profiles show a similar behaviour to those of water, evolving from pure absorption or P-Cygni at shorter wavelengths to pure emission at longer wavelengths.

Table 7 lists a comparison of the fluxes and surface brightnesses of seven OH transitions measured with different beam sizes by different observers.

A similar behaviour to that of the water line velocities is also found for the OH detections, showing center velocities between -10 km s^{-1} and $+30 \text{ km s}^{-1}$ (see Section 4.4) when the line appear in absorption or emission respectively. Radiative transfer modelling has been recently performed for the OH lines (Goicoechea et al. 2006) and concludes that most of the newly detected excited OH lines in the survey originate in a compact region ($D \approx 25''$), not resolved by the LWS, that forms part of the low velocity plateau component. Average values of the physical conditions in this region are estimated to be: $n(\text{H}_2) \approx 5 \times 10^5 \text{ cm}^{-3}$, $T_k \approx 100 \text{ K}$ and an abundance of $\chi(\text{OH}) \approx (0.5 - 1) \times 10^{-6}$.

4.3.4 OH isotopes

The detection of ${}^{18}\text{OH}$ at the sensitivity of the FP-LWS observations was found to be very difficult. The weakness of the lines makes them easily confused with noise and only the ${}^{18}\text{OH } {}^2\Pi_{3/2} 5/2^+ \rightarrow 3/2^-$ transition at 119.96 μm and the ${}^2\Pi_{3/2} 5/2^- \rightarrow 3/2^+$ transition at 120.17 μm were tenta-

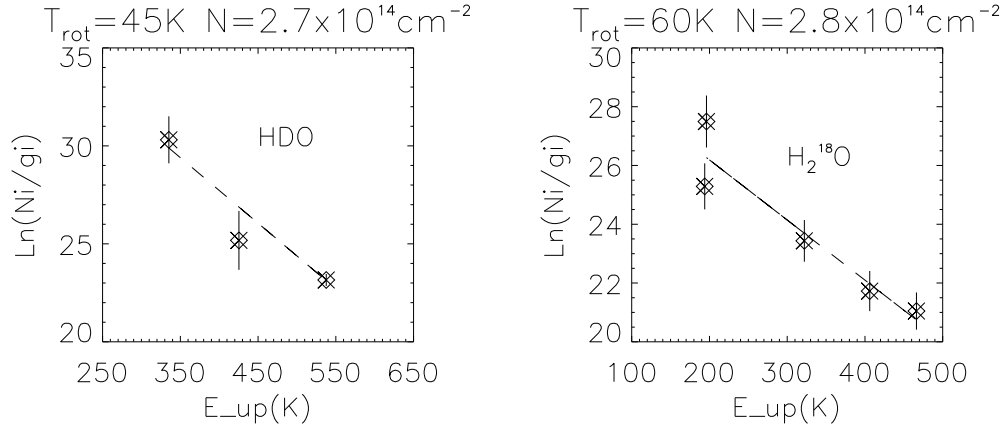


Figure 12. Rotational diagrams i.e. the natural logarithm of the column density in the i th stage, N_i , divided by the degeneracy g_i versus the upper energy E_{up} for the HDO and $H_2^{18}O$ transitions detected by the survey towards Orion KL. Due to the high uncertainties of the high energy HDO lines, only the lowest energy transitions are considered. Note also that P-Cygni lines are excluded from the diagram.

Line	Wavelength (μm)	FWHM Beam Size (arcsec)	Reference ^(a)	Flux ($10^{-17} W cm^{-2}$) ^(b)	Surface Br. ($10^{-3} ergs cm^{-2} s^{-1} sr^{-1}$)
$^2\Pi_{1/2} J=3/2^- \rightarrow 1/2^+$	163.396	67	1	1.66 ± 0.38	2.04
		55	2	1.3	1.6
		60	2	1.2 ± 0.6	1.2
$^2\Pi_{1/2} J=3/2^+ \rightarrow 1/2^-$	163.121	67	1	0.81 ± 0.19	0.99
		55	2	1.3	1.6
		60	2	1.2 ± 0.6	1.2
$^2\Pi_{3/2} J=5/2^+ \rightarrow 3/2^-$	119.441	78	1	2.42 ± 0.13	2.16
		44	4	0.7 ± 0.3	1.3 ± 0.5
$^2\Pi_{3/2} J=5/2^- \rightarrow 3/2^+$	119.234	78	1	1.76 ± 0.17	1.57
		44	4	0.83	1.5
		45	5	1.88	3.3
$^2\Pi_{3/2} J=7/2^- \rightarrow 5/2^+$	84.597	77	1	$(1.13 \pm 0.38)^{abs}$	1.01^{abs}
				$(1.34 \pm 0.26)^{em}$	1.19^{em}
		30	4	0.56	2.1
$^2\Pi_{3/2} J=7/2^+ \rightarrow 5/2^-$	84.420	60	3	1.4 ± 0.4	1.4
		77	1	1.72 ± 0.13	1.54
		30	4	<0.5	<1.9
$^2\Pi_{1/2} J=3/2^- \rightarrow ^2\Pi_{3/2} J=3/2^+$	53.351	60	3	1.0 ± 0.3	1.0
		85	1	$(2.45 \pm 0.26)^{abs}$	1.86^{abs}
				$(0.26 \pm 0.13)^{em}$	0.19^{em}
		40	5	3.00^{abs}	6.6^{abs}
				0.63^{em}	1.4^{em}

^(a) References :

1 Values using *ISO* LWS
data in this work

2 Melnick et al. 1987

3 Viscuso et al. 1985

4 Watson et al. 1985

5 Melnick et al. 1990

^(b)

^(abs) P Cygni

absorption component

^(em) P Cygni

emission component

Table 7. Comparison of OH line measurements obtained with different beam sizes and instruments. The uncertainty in the absolute fluxes and intensities is $\pm 30\%$ unless indicated otherwise

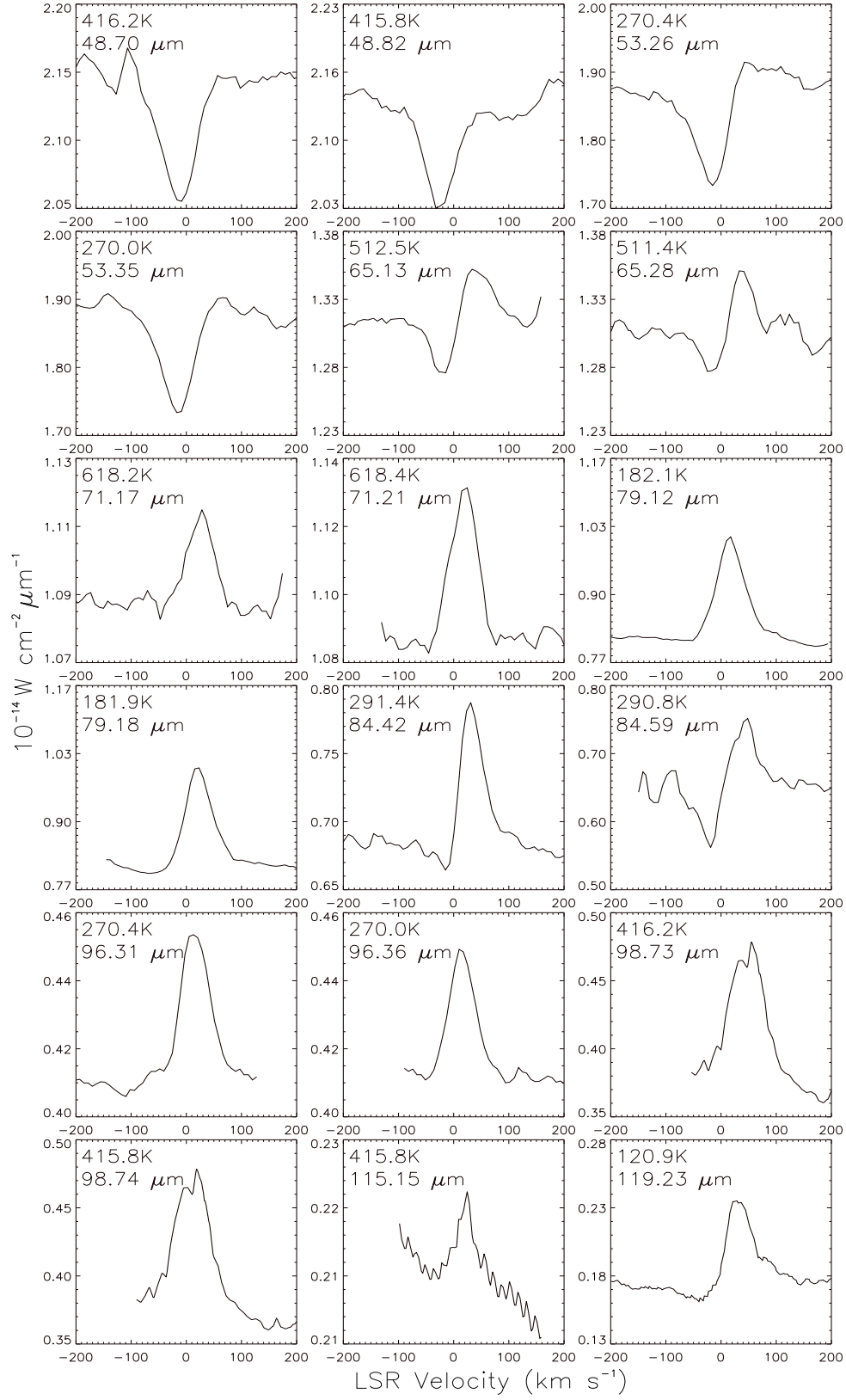


Figure 13. OH lines observed in the survey

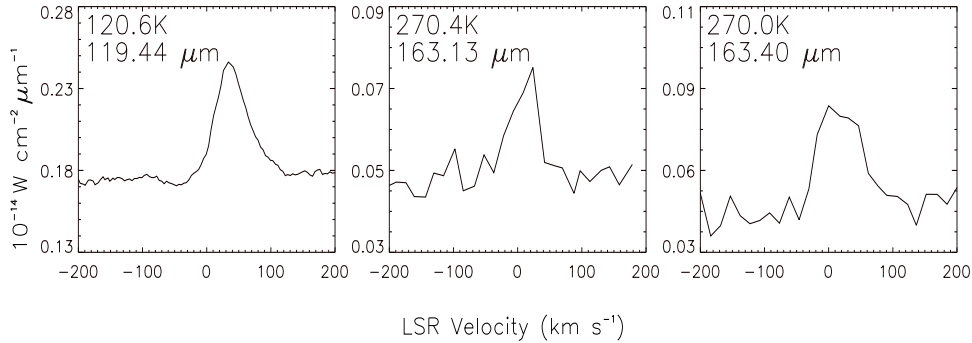


Figure 13. Continued

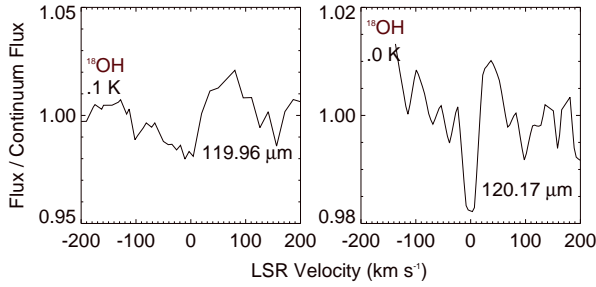


Figure 14. ^{18}OH lines observed in the survey towards Orion KL. The left plot is the $^2\Pi_{3/2} \ 5/2^+ \rightarrow 3/2^-$ transition at $119.96 \ \mu\text{m}$ and the right plot is the $^2\Pi_{3/2} \ 5/2^- \rightarrow 3/2^+$ transition at $120.17 \ \mu\text{m}$.

tively identified (see Figure 14).

As with water, isotopic variants play an important role in the interpretation of the OH lines. Both ^{18}OH transitions detected show a difference in their line profiles when compared with their corresponding ^{16}OH transitions. As the ^{18}OH optical depths are smaller than those measured for the ^{16}OH transitions, and since both line profiles are P-Cygni, the ^{18}OH lines indicate that OH is predominantly associated with the Plateau outflow (see also Goicoechea et al. 2006).

4.3.5 CO emission lines

High-J CO transitions are well known among the most common tracers of highly excited regions. OH and H_2O can react with C^+ via the reactions:



These reactions are sufficiently rapid to ensure that substantial amounts of CO are produced in shocks (Pineau des Forêts et al. 1986, 1987)

Watson et al. (1980) made the first far-infrared detection of interstellar CO with observations of the $J=21-20$ and $J=22-21$ transitions at $124 \ \mu\text{m}$ and $119 \ \mu\text{m}$ respectively,

from the BN/KL region. Using collisional excitation cross sections calculated by Storey et al. (1981), they derived CO rotational level populations for a number of temperatures and densities. They showed that the observed line intensities could be modelled by emission from two components: a 2000 K component with $n(\text{H}_2) \sim 1 \times 10^6 \text{ cm}^{-3}$ and a 400 – 1000 K component with $n(\text{H}_2) \sim 5\text{--}2 \times 10^6 \text{ cm}^{-3}$. More recent studies using *ISO* data indicate that the CO emission can be modelled using three temperature components, describing the plateau and the ridge emission (Sempere et al. 2000, Maret et al. 2001)

CO detections originating from $J_{up}=14$ to $J_{up}=52$ are identified by our survey in a total of 26 detected emission lines. Line profiles are shown in Figure 15 and the measured line fluxes and intensities are compared in Table 8 with those measured by Storey et al. (1981) and Watson et al. (1985) using the *KAO*. Note that the field of view for *KAO*'s observations was 60 arcsec for the $J_{up} = 17, 16$ lines and ~ 44 arcsec for the $J_{up} = 21, 22, 26, 27, 30$ and 31 lines. An interesting result from Table 8 is that almost identical surface brightnesses were measured for the $J=17-16$ and $J=16-15$ transitions when observed with the $60''$ *KAO* beam and the $80''$ LWS beam. However for the higher J CO lines we find that the surface brightness in the $44''$ *KAO* beam is about 60% higher than in the $80''$ LWS beam, while the integrated fluxes in the two beam sizes are similar, indicating that the source size may be smaller than 44 arcsec for these transitions.

CO is also an important tracer of H_2 , since it is the second most abundant molecule in the interstellar medium after molecular hydrogen. Despite theoretical and observational uncertainties in the use of a canonical $N(\text{CO})/N(\text{H}_2)$ ratio (Williams et al. 1984; van Dishoeck et al. 1992; Sakamoto et al. 1996), theoretical studies of the CO/ H_2 abundance ratio have concluded that on large scales it can be considered to be constant (Taylor et al. 1993).

In Figure 16 we show rotational diagrams for three different CO J-ranges, finding three different rotational temperatures. Below, we compare our results with the model of Sempere et al. (2000) which was developed using a radiative transfer model fit to *ISO* data obtained at low spectral resolution (grating mode), together with selected observations at high spectral resolution. In this model:

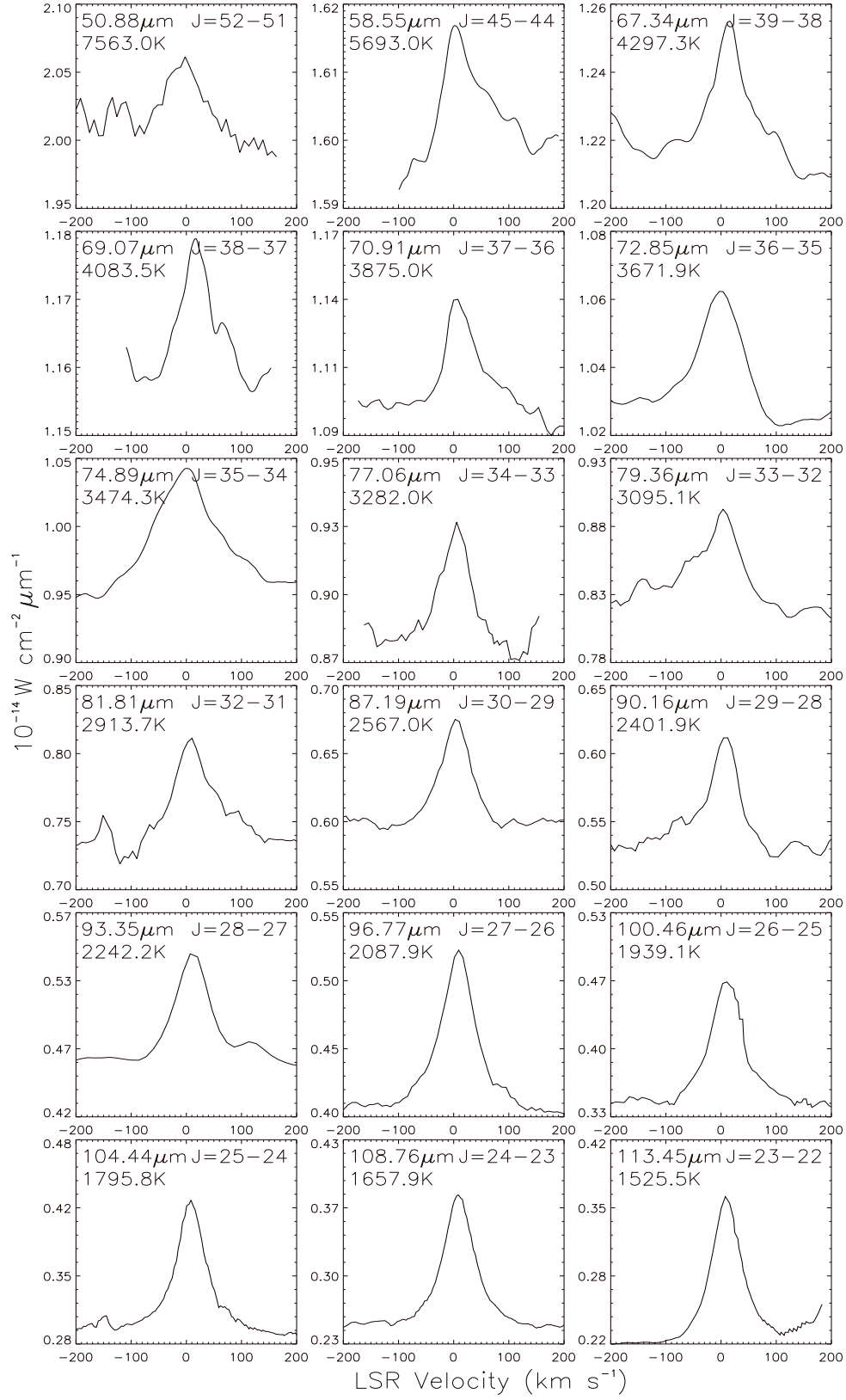


Figure 15. CO lines detected by the survey

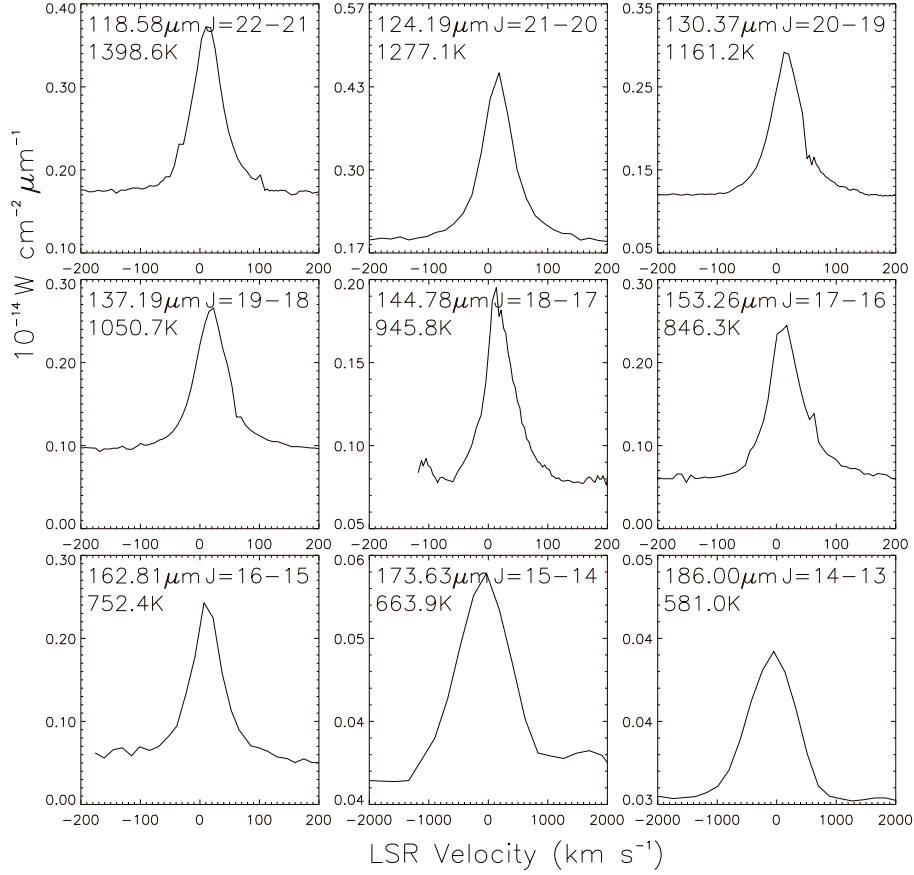


Figure 15. continued

- The CO emission from $J=18$ to 33 can be explained by a two temperature component model of the plateau region; the inner region reproduces the emission from $J=33$ to 28 and the colder gas contributes to the lower J lines. The high J transitions ($J > 34$) reveal the presence of a very hot gas component ($T \approx 1500\text{--}2000\text{K}$).

- They assumed densities of 10^7 cm^{-3} and a temperature of 400 K for the inner region and 10^6 cm^{-3} , 300K for the external part of the plateau.

- The resulting column densities in Sempere et al's model were: $N(\text{CO})=10^{19} \text{ cm}^{-2}$ and $N(\text{CO})=3.5 \times 10^{18} \text{ cm}^{-2}$ for the inner and outer plateau, and $N(\text{CO})=10^{17} \text{ cm}^{-2}$ for the hot gas component.

The results from our rotational diagrams shows consistency with the different temperature components predicted by Sempere et al's model. Our results confirm the presence of hot gas ($T \approx 660 \text{ K}$; Figure 16) which differs by $\approx 300 \text{ K}$ from the warm component ($T \approx 360 \text{ K}$, see Figure 16). However, we found that this warm component has a higher CO column density than that found by Sempere et al., with a column density of the order of $\approx 2.3 \times 10^{19} \text{ cm}^{-2}$. According to our results, the inner part of the Plateau component is traced by the warm gas which emits the CO transitions with $J < 28$ with a rotational temperature of $\approx 360 \text{ K}$.

4.3.6 CO isotopic variants

CO isotopic variants are hardly detected in the survey. Only one line of ^{13}CO (the $J = 21\text{--}20$ transition at $129.89 \mu\text{m}$) is tentatively detected with a flux of $2 \pm 1 \times 10^{-19} \text{ W cm}^{-2}$.

4.4 Line kinematics

Although kinematical properties are diluted in the large LWS beam, resolved line profiles and velocity peaks can trace the overall dynamical gas properties. Figure 17 shows the upper transition energy of the main molecular detections of H_2O , OH and CO , as a function of the emission and absorption LSR line velocity peaks. For the H_2O and OH lines, both pure emission or absorption and P-Cygni peaks are plotted. The velocity of the quiescent gas is $9.0 \pm 0.5 \text{ km s}^{-1}$ (Cohen et al. 2006). Subtracting this value from the velocity peaks gives an indication of the exact blue- or red-shift of the lines. Several conclusions can be deduced from Figure 17:

- H_2O and OH radial velocities trace the velocity distribution of the same expanding gas. Absorption lines are centred between -15 and -30 km s^{-1} and emission lines between $+15$ and $+45 \text{ km s}^{-1}$. This confirms previous analyses of these lines (Harwit et al. 1998; Cernicharo et al. 1999; Goicoechea et al. 2006) which interpreted them as evidence

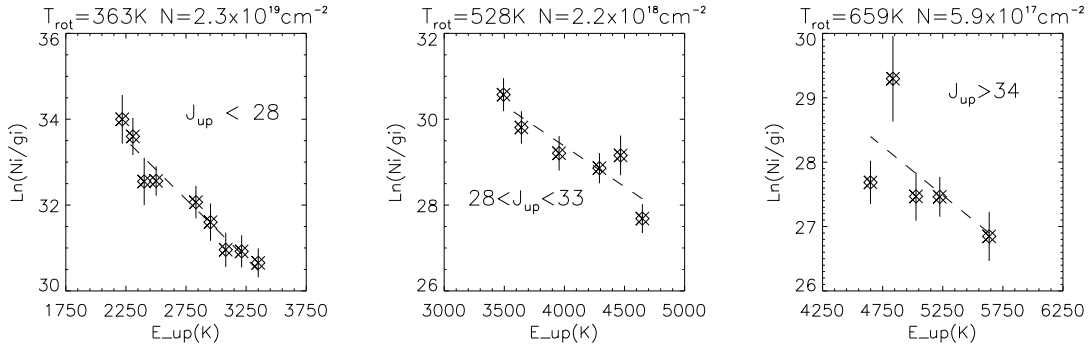


Figure 16. Rotational diagrams i.e. the natural logarithm of the column density in the i th stage, N_i , divided by the degeneracy g_i versus the upper energy E_{up} for the observed CO emission towards Orion KL using *ISO* LWS-FP data.

Transition	λ (μm)	LWS Flux ^a [10^{-17}W cm^{-2}]	LWS Intensity ^a [$10^{-3}\text{ergs}^{-1}\text{cm}^{-2}\text{sr}^{-1}$]	KAO Flux ^b [10^{-17}W cm^{-2}]	KAO Intensity ^b [$10^{-3}\text{ergs}^{-1}\text{cm}^{-2}\text{sr}^{-1}$]
J=34–33	77.05	0.60	0.52	0.43	0.86
J=30–29	87.19	1.58	1.37	1.6	2.41
J=27–26	96.77	3.82	3.47	4.3	6.47
J=26–25	100.46	3.44	3.13	1.9	3.80
J=22–21	118.58	6.58	5.87	5.3	11.0
J=21–20	124.19	7.89	8.87	6.8	10.2
J=17–16	153.27	8.66	10.35	7.0 ^c	10.5
J=16–15	162.81	9.48	9.88	6.4 ^c	9.63

(a) Line fluxes and intensities averaged over a $80''$ beam observed by the *ISO* LWS in Fabry-Pérot mode.

(b) Line fluxes and intensities averaged over a $44''$ beam measured by Watson et al. (1981) using the UC Berkeley tandem Fabry-Pérot spectrometer.

(c) Storey et al. (1981) using a $60''$ beam.

Table 8. LWS Fabry-Pérot CO detections towards Orion KL, compared with those of Watson et al. (1981)

for outflows driven by the star formation activity of Orion KL.

- For H_2O and OH , the absorption and emission components of the P-Cygni lines tend to be at more extreme velocities than those of the ‘pure’ absorption or emission lines. Detailed radiative transfer modelling is underway to attempt to match this behaviour.

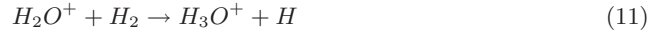
- The CO radial velocities indicate a different excitation mechanism to that of H_2O and OH , with emission peaks centred between $(5 - 15) \text{ km s}^{-1}$. Considering an average velocity uncertainty of $\pm 10 \text{ km s}^{-1}$, this range is consistent with the velocity of the quiescent gas ($\approx 9 \text{ km s}^{-1}$). As very high energy CO transitions are detected, the lines may originate in the hot and warm quiescent post-shocked gas.

4.5 H_3O^+ line detections

H_3O^+ is one of the key species in the interstellar chemistry of oxygen. This saturated molecular ion leads to the formation of OH and H_2O by dissociative recombination, with an imprecisely known branching ratio (Bates 1986; Sternberg 1995). It can be formed from H_3^+ by the reaction:



or via the reactions:



Its formation is more likely to occur via reactions 9–11 (Wootten et al. 1986). Destruction of H_3O^+ occurs via electron recombination:



leading to the production of H_2O and OH .

H_3O^+ has a pyramidal structure; inversion transitions are produced when the oxygen atom tunnels through the plane of the hydrogen atoms. The ground state inversion splitting is $\approx 55 \text{ cm}^{-1}$ (Liu et al. 1985). This large value makes the fundamental transitions of the ν_2 mode lie at submillimeter and far-infrared wavelengths (Wootten et al. 1986, Bogey et al. 1985). H_3O^+ was first detected at 365 GHz in OMC-1 and Sgr B2 by Wootten et al. (1991) and more recently in the far-infrared towards Sgr B2 (Goicoechea and Cernicharo, 2001; Polehampton et al. 2006). Wootten et al. (1991) modeled the excitation of the para- H_3O^+ transition at 365 GHz, finding abundances $\chi(\text{H}_3\text{O}^+) \approx 1 \times 10^{-9} \rightarrow 5 \times 10^{-9}$.

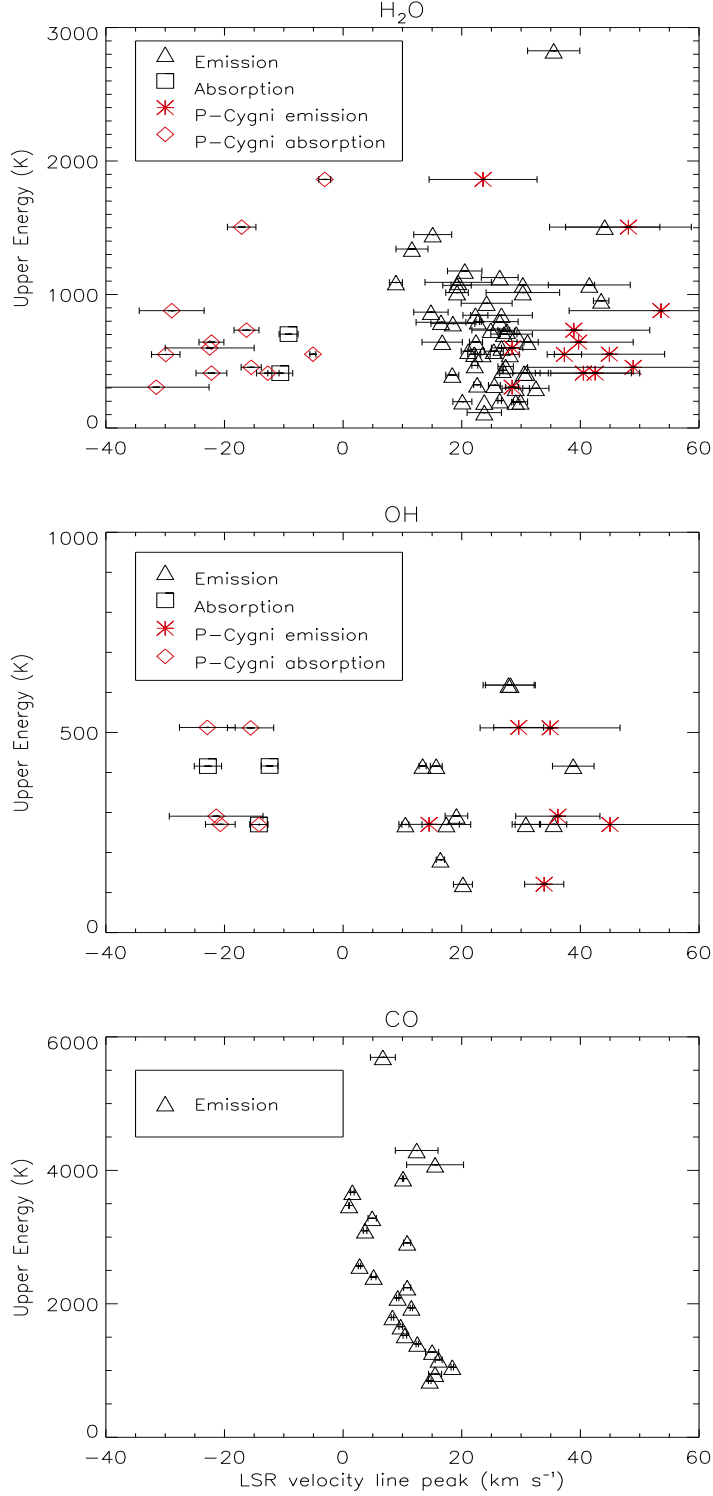


Figure 17. LSR peak velocities of H₂O, OH and CO lines observed towards Orion KL with the *ISO* LWS-FPs. Note that the LSR velocity of the quiescent gas is ≈ 9 km s⁻¹ LSR (Cohen et al. 2006). Errors are from goodness of fit estimations.

The lowest rotational levels of the ortho and para ladders of the ν_2 ground-state H₃O⁺ inversion mode ($0^+ \rightarrow 0^-$) are detected in the survey. These are the rotational inversions $2_1^- \rightarrow 1_1^+$ at $100.58 \mu\text{m}$ and $2_0^- \rightarrow 1_0^+$ at $100.87 \mu\text{m}$ and the pure inversion $1_1^- \rightarrow 1_1^+$ transition at $181.05 \mu\text{m}$ (see Fig-

ure 18). The optical depths of these transitions estimated with the RADEX code are $\tau > 10$. We used as input the column density values inferred by Wootten et al. (1991; $\approx 10^{14} \text{ cm}^{-2}$), $T_K = 80$ K and $n_{\text{H}_2} = 10^5 \text{ cm}^{-3}$. The rotational diagram method cannot therefore be applied to derive phys-

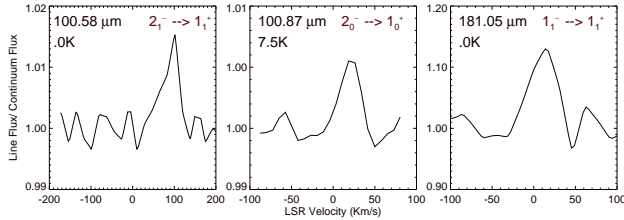


Figure 18. H_3O^+ lines observed towards Orion KL

ical parameters. Further modelling of optically thick lines including radiative excitation by the FIR dust continuum emission is needed and will be published in forthcoming papers.

4.6 NH_3 line detections

Like H_3O^+ , the NH_3 molecule has a pyramidal structure. Inversion transitions are produced when the nitrogen atom tunnels through the plane of the hydrogen atoms (analogous to the tunnelling of the O atom in H_3O^+), with the significant difference that the inversion splitting $\approx 1 \text{ cm}^{-1}$, much smaller than that of H_3O^+ (Ho & Townes, 1983).

NH_3 was first detected at far-IR wavelengths by the KAO towards Orion-KL (Townes et al. 1983), in the rotational $\nu_2=1$; $4_3^- - 3_3^+$ line at $124.6 \mu\text{m}$. The fact that this line is very optically thick ($\tau \approx 10^3$) and that it is seen in emission, led the authors to consider that this level is collisionally excited, probably originating in the Hot Core component.

The $4_3^- - 3_3^+$ transition at $124.6 \mu\text{m}$ is also detected by the LWS, as well as the following transitions: $4_2^- - 3_2^+$ $124.8 \mu\text{m}$, $4_0^- - 3_0^+$ $124.9 \mu\text{m}$ and $3_2^- - 2_2^+$ $165.6 \mu\text{m}$ (see Figure 19).

We estimated the optical depths of these transitions with the RADEX code, using as input the inferred column density of 10^{14} cm^{-2} , $T_K=80\text{K}$ and $n_{\text{H}_2}=10^5 \text{ cm}^{-3}$. For these conditions, only the $3_2^- - 2_2^+$ transition at $165.6 \mu\text{m}$ is moderately optically thick ($\tau = 1.4$). Figure 20 shows the rotational diagram of NH_3 , with an inferred column density of $1.3 \times 10^{14} \text{ cm}^{-2}$ and a rotational temperature of 40 K. However, if the NH_3 column density is $\geq 10^{15} \text{ cm}^{-2}$ the code predicts high optical depths and our rotational calculation could be underestimated. Estimations of the NH_3 abundance using more sophisticated models will be published in forthcoming papers.

4.7 Unidentified and weak features

Some isotopic lines that were detected by the LWS in L04 mode were very difficult to detect in the L03 scans, due to differences between repeated scans. This affected the detection of weak transitions. However, some unidentified lines were detected after carrying out an exhaustive analysis, in which the lines were seen in at least two different observations plotted together in order to discriminate between glitches and spurious features. The observations were also analyzed before performing smoothing corrections, to ensure that no features were missed in this step. Table 10 gives a list of the unidentified features found in the survey. The line fluxes were derived using similar fits to those used for iden-

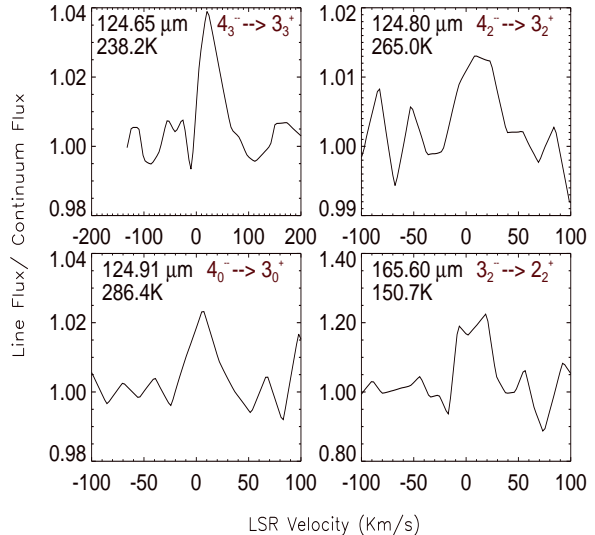


Figure 19. NH_3 lines observed towards Orion KL

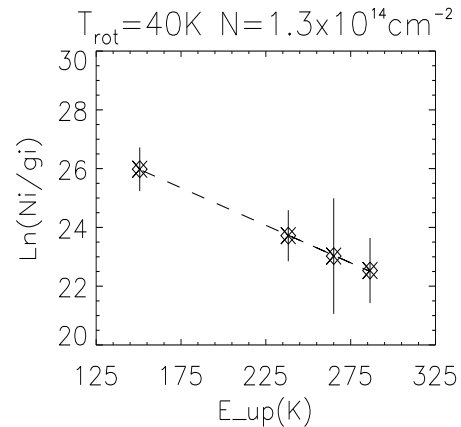


Figure 20. Rotational diagram for the NH_3 lines detected towards Orion KL.

tified lines.

Amongst the candidate detections are several rotational transitions of the H_2O vibrational bending mode ν_2 (44.09 and $84.36 \mu\text{m}$). There are also many rotational transitions in the far-IR of slightly asymmetrical species that could be contributing to the spectrum but may not have been detected at the FP resolution, such as HNO , HNCO or HOCO^+ and the low-energy bending modes of carbon chains.

5 CONCLUSIONS

A high spectral resolution $44\text{--}188 \mu\text{m}$ line survey towards Orion KL has been carried out with the ISO LWS in Fabry-Pérot mode. A total of 152 lines are identified and a further 34 lines remain to be identified. A basic analysis of the molecular detections was carried out by deriving rotational temperatures and column densities (see summary in

Molecule	Method	N_{col} cm ⁻²	T_{rot} K	Lines	Note
CO	1	$(1-3) \times 10^{19}$	360	15	Inner Plateau
CO	1	$(1-4) \times 10^{18}$	530	5	Plateau
CO	1	$(2-7) \times 10^{17}$	660	5	Hot Gas
¹³ CO				1	
OH	2	$(2.5-5.1)^{(a)} \times 10^{16}$		22	Low velocity Plateau
H ₂ O	3	$(1-3) \times 10^{17}$	60	70	
HDO	1	$(1-5) \times 10^{14}$	45	5	
H ₂ ¹⁸ O	1	$(2-5) \times 10^{14}$	60	5	
H ₂ ¹⁷ O				1	
NH ₃	1	$(1-5) \times 10^{14}$	40	4	
H ₃ O ⁺				3	

Table 9. Rotational temperatures and beam averaged column densities N_{col} , estimated using LTE rotational diagram method or using non-Local radiative transfer models, for the different molecular species identified in the far-infrared survey towards Orion KL with *ISO* LWS-FP data. Column 2 list the method used to estimate the column density; [1] rotational diagram method, [2] non-Local radiative transfer models, [3] via the isotopic ratio.^(a) From Goicoechea et al. 2006

Wavelength observed (μ m)	Flux (10^{-18} W cm ⁻²)	absorption	emission
44.09 \pm 7.5 $\times 10^{-3}$	1.54 \pm 0.98		X
46.29 \pm 5.5 $\times 10^{-4}$	1.46 \pm 0.31		X
48.48 \pm 5.5 $\times 10^{-4}$	6.36 \pm 1.82		X
48.75 \pm 1.1 $\times 10^{-3}$	2.58 \pm 0.83		X
52.29 \pm 5.7 $\times 10^{-4}$	4.14 \pm 1.61		X
52.57 \pm 9.5 $\times 10^{-4}$	6.07 \pm 2.01		X
58.02 \pm 8.5 $\times 10^{-3}$	1.44 \pm 0.38	X	
58.24 \pm 5.5 $\times 10^{-3}$	1.67 \pm 0.53		X
63.78 \pm 3.6 $\times 10^{-4}$	5.06 \pm 1.06		X
64.34 \pm 9.5 $\times 10^{-3}$	0.87 \pm 0.27		X
66.63 \pm 8.5 $\times 10^{-4}$	2.03 \pm 0.74		X
67.14 \pm 4.5 $\times 10^{-3}$	1.55 \pm 0.75		X
68.61 \pm 8.8 $\times 10^{-3}$	1.98 \pm 0.47		X
84.36 \pm 5.5 $\times 10^{-3}$	1.57 \pm 0.93		X
91.13 \pm 7.5 $\times 10^{-3}$	0.36 \pm 0.15		X
91.97 \pm 3.2 $\times 10^{-4}$	4.08 \pm 0.10		X
101.78 \pm 4.1 $\times 10^{-4}$	0.31 \pm 0.10		X
104.39 \pm 5.6 $\times 10^{-3}$	0.68 \pm 0.37		X
108.30 \pm 2.2 $\times 10^{-4}$	0.32 \pm 0.05		X
112.82 \pm 5.4 $\times 10^{-3}$	0.29 \pm 0.14		X
114.96 \pm 7.5 $\times 10^{-3}$	0.27 \pm 0.093		X
115.68 \pm 2.5 $\times 10^{-3}$	0.41 \pm 0.22		X
116.27 \pm 6.9 $\times 10^{-4}$	0.89 \pm 0.24		X
116.60 \pm 9.5 $\times 10^{-3}$	0.49 \pm 0.35		X
122.37 \pm 4.4 $\times 10^{-4}$	1.21 \pm 0.027	X	
123.80 \pm 2.7 $\times 10^{-4}$	7.40 \pm 0.088		X
126.64 \pm 8.5 $\times 10^{-3}$	0.19 \pm 0.056		X
131.44 \pm 9.5 $\times 10^{-4}$	1.23 \pm 0.45		X
133.34 \pm 3.2 $\times 10^{-3}$	0.76 \pm 0.36		X
136.61 \pm 2.3 $\times 10^{-3}$	0.69 \pm 0.20		X
137.50 \pm 8.4 $\times 10^{-3}$	0.99 \pm 0.48		X
139.54 \pm 4.8 $\times 10^{-3}$	1.66 \pm 0.065		X
140.60 \pm 8.6 $\times 10^{-3}$	0.33 \pm 0.15		X
144.47 \pm 5.9 $\times 10^{-4}$	4.11 \pm 0.86		X

Table 10. List of unidentified and weak features found on the survey towards Orion KL with *ISO* high resolution spectra Fabry-Pérot mode. The unidentified line selection criteria was based on the features that were seen in at least two different observations plotted together in order to discriminate between glitches and spurious features. The observations were also analysed before performing smoothing corrections, to assure that no features were missed in this step.

Table 9) and by comparison with previous measurements and published models. We found that:

- The spectrum is dominated by the main molecular coolants: H_2O , CO and OH together with the forbidden lines $[\text{O I}]$, $[\text{O III}]$, $[\text{N III}]$ and $[\text{C II}]$.
- The analysis of the $[\text{O I}]$ and $[\text{C II}]$ fine structure lines indicates that a PDR model can reproduce the observed $[\text{O I}]$ 63.2 μm and $[\text{C II}]$ 157.7 μm surface brightness levels although it over-predicts the $[\text{O I}]$ 145.5 μm emission by a factor of 2.7.
- The water and OH P-Cygni profiles, along with the kinematical line properties, confirm that most of the detected emission is associated with gas expanding in the outflow from the KL cluster.
- The observed molecular emission is consistent with previous models where several main components were clearly distinguished; the CO detections confirm the differentiation into physically distinct components, with column densities ranging from $\approx 10^{19}$ to $\approx 10^{17} \text{ cm}^{-2}$ and temperatures from 350 to 650 K.
- HDO and H_3O^+ are tentatively detected for the first time in the far-infrared range towards Orion KL. The derived HDO column density ($\approx 10^{14} \text{ cm}^{-2}$) is lower than the values (10^{16} cm^{-2}) obtained at millimeter and submillimeter wavelengths. Due to the high optical depths of the lines, more sophisticated non-local radiative transfer models are needed to estimate the H_3O^+ and NH_3 column densities.

The 80 arcsec *ISO* LWS beam size encompasses a large range of physical conditions, ranging from quiescent cool gas to outflows that alter the chemistry of the region. Consequently, the exact interpretation of the line survey requires modelling. We plan to model the chemistry and dynamics of the main components using a coupled chemical-radiative transfer code.

ACKNOWLEDGEMENTS

The authors would like to thank Glenn White and the anonymous referee for their suggestions and helpful comments. The *ISO* Spectral Analysis Package (ISAP) is a joint development by the LWS and SWS Instrument Teams and Data Centres. Contributing institutes are CESR, IAS, IPAC, MPE, RAL and SRON. LIA is a joint development of the *ISO*-LWS Instrument Team at Rutherford Appleton Laboratories (RAL, UK- the PI institute) and the Infrared Processing and Analysis Center (IPAC/Caltech, USA). JRG was supported by a Marie Curie Intra-European Fellowship under contract MEIF-CT-2005-515340 within the 6th European Community Framework programme.

REFERENCES

- Bates, D. R., 1986, *ApJ*, 306, 45
- Blake, G. A., Sutton, E. C., Masson, C. R., & Phillips, T. G., 1986, *ApJ*, 60, 257
- Blake, G. A., Sutton, E. C., Masson, C. R., & Phillips, T. G., 1987, *ApJ*, 315, 621
- Becklin, E. E. & Neugebauer, G., 1967, *ApJ*, 147, 799
- Beckman, J. E., Watt, G. D., White, G. J., Phillips, J. P., Frost, R. L., Davis, J. H., 1982, *MNRAS*, 201, 357
- Bergin, E. A., Plume, R., Williams, P. & Myers, P. C., 1998, *ApJ*, 512, 724
- Bogey, M., Demuynck, C., Denis, M., & Destombes, J. L., 1985, *A&A*, 148, 11
- Cernicharo, J. & Crovisier, J., 2005, *Space Science Reviews*, 119, 29
- Cernicharo, J., Gonzalez-Alfonso, E., Alcolea, J., Bachiller, R., et al., 1994, *ApJ*, 432, 59
- Cernicharo, J., Gonzalez-Alfonso, E., Sempere, M. J., Leeks, S. J., van Dishoeck, E. F., et al., 1999, in *The Universe Seen by ISO*, Eds. P. Cox & M. F. Kessler, ESA-SP 427, 565
- Cernicharo, J., Thum, C., Hei, H., John, D., et al., 1990, *A&A*, 231, 15
- Chandler, C. J. & Greenhill, L. J., 2002, *SPC*, 267, 357
- Chandra, S., 1985, *A&A*, 59, 59
- Chandra, S., Maheshwari, V. U., Sharma, A. K., 1996, *A&A*, 117, 557
- Chandra, S., Kegel, W. H. & Varshalovich, D. A., 1984, *A&A*, 58, 687
- Chernoff, D. F., McKee, C. F., Hollenbach, D. J., 1982, *ApJ*, 259, 97
- Clegg, P. E., Ade, P. A. R., Armand, C., Baluteau, J.-P., et al., 1996, *A&A* 315, L38
- Cohen, R. J., Gasipron, N., Meaburn, J. & Graham, M. F., 2006, *MNRAS*, in press.
- Comito, C., Schilke, P., Phillips, T. G., Lis, D. C., Motte, F., Mehringer, D., 2005, *A&A*, 156, 127
- Cox, J. P. 1980, *Theory of Stellar Pulsation* (Princeton University Press, Princeton) 165
- Dougados, C., Lena, P., Ridgway, S. T., Christou, J. C. & Probst, R. G., 1993, *ApJ*, 406, 112
- Downes, D., Genzel, R., Becklin, E. E., & Wynn-Williams, C. G. 1981, *ApJ*, 244, 869
- Draine, B. T., & Roberge, W. G., 1982, *ApJ*, 259, 91
- Elitzur, M., & Watson, W. D., 1978, *A&A*, 70, 443
- Ellis, H. B., and Werner, W. M., 1985, *mlrg, proc.*, 117, 309
- Furniss, I., Jennings, R. E., King, K. J., Lightfoot, J. F., Emery, R. J., et al., 1983, *MNRAS*, 202, 859
- Genzel, R., Reid, M. J., Moran, J. M. and Downes, 1981, *ApJ*, 244, 844
- Genzel, R., & Stutzki, J., 1989, *A&A*, 27, 41
- Gezari, D. Y., Backman, D. E., & Werner, M. W., 1998, *ApJ*, 509, 283
- Goicoechea, J., & Cernicharo, J., 2001, *ApJ*, 554, 213
- Goicoechea, J. R., Cernicharo, C., Lerate, M. R., Daniel, F., et al., 2006, *ApJ*, astro. ph, 3077
- Greaves, J. S. & White, G., J., 1991, *A&A*, 248, 27
- Gry, C., Swinyard, B., Harwood, A., Trams, N., et al. 2003, *ISO Handbook Volume III(LWS)*, Version 2.1, ESA SAI-99-07.
- Harwit, M., Neufeld, D., Melnick, G. J., Kaufman, M. J., 1998, *ApJ*, 497, 105
- Hecht, E. & Zajac, A., 1974, *Optics*, Addison-Wesley
- Ho, P. T. P. & Townes, C. H., 1983, *A&A*, 21, 239
- Hollenbach, D. & McKee, C. F., 1989, *ApJ*, 342, 306
- Johansson, L. E. B., Andersson, C., Ellder, J., Friberg, P., et al., 1984, *A&A*, 130, 227
- Kleinmann, D. E., & Low, F. J., 1967, *ApJ*, 149, L1

- Leeks, S.J., Swinyard, B.M., Lim, T., et al. 1999, *ESA SP-427*, 81
- Lim, T.L., Hutchinson, G., Sidher, S.D., Molinari, S., et al. 2002, *SPIE*, 4847, 435
- Lis, D. C., Serabyn, E., Keene, J., Jocelyn, D. C., et al., 1998, *ApJ*, 509,229
- Liu, D. J., Oka, T., 1985, *Phys. Rev. Lett.*, 54, 1787
- Liu, X. W., Barlow, M. J., Cohen, M., Danziger, I. J., et al. 2001, *MNRAS*, 323, 343
- Lloyd, C., 1993, *clim.*, conf., 399
- Lloyd, C., Lerate, M.R., & Grundy, T.W. 2003, *The LWS L01 Pipeline*, version 1, available from the *ISO Data Archive* at <http://www.iso.vilspa.esa.es/ida/>
- Lynds, B. T., 1962, *ApJS*, 7, 1
- Maret, S., Caux, E., Baluteau, J.-P., Ceccarelli, C., Gry, C., Vastel, C., 2001, *ESA SP-460*, 455
- Melnick, G. J., Gull, G. E., & Harwit, M., 1979, *ApJ*, 227, 29
- Melnick, G. J., Genzel, R., & Lugten, J. B., 1987, *ApJ*, 321, 530
- Melnick, G. J., Stacey, G. J., Genzel, R., Lugten, J. B. and Poglitsch, A., 1990, *ApJ*, 348, 161
- Menten, K. M., & Reid, M. J. 1995, *ApJ*, 445, L157
- Moore, E. L., Huguenin, G. R., Langer, W. D., 1986, *ApJ*, 306, 682
- Neufeld, D. A., & Melnick, G. J., 1987, *ApJ*, 332, 266
- Pardo, J. R., Cernicharo, C. & Herpin, F., 2001, *ApJ*, 562, 799
- Petuchowski, S. J., Bennett, C. L., 1993, *ApJ*, 405, 591
- Phillips, T. G., & Huggins, P. J., 1981, *ApJ*, 251, 553
- Pickett, H. M., R. L. Poynter, E. A. Cohen, M. L. Delitsky, et al., 1998, *Submillimeter, Millimeter and Microwave Spectral Line Catalog*, *J. Quant. Spectrosc. & Rad. Transfer*, 60, 883
- Pineau des Forêts, G., Flowers, D. R., Hartquist, T. W. & Dalgarno, A., 1986, *MNRAS*, 220, 801
- Pineau des Forêts, G., Flowers, D. R., Hartquist, T. W. & Millar, T. J., 1987, *MNRAS*, 227, 993
- Polehampton, E. T. 2002, PhD thesis, Oxford University
- Polehampton, E. T., Brown, J. M., Swinyard, B. M., & Baluteau, J. P., 2003, *A&A*, 406, L47
- Polehampton E. T., Baluteau, J. P., Swinyard, B. M., Goicoechea, J. R., et al., 2006, *MNRAS*, in prep.
- Rubin, R. H., Simpson, J. P., Lord, S. D. et al., 1994, *ApJ*, 420, 772
- Russell, R. W., Melnick, G., Gull, G. E., & Harwit, M., 1980, *ApJ*, 240, 99
- Sakamoto, S, 1996, *ApJ*, 462, 215
- Schilke, P., Benford, D. J., Hunter, T. R., Lis, D. C., & Phillips, T. G., 2001, *ApJ*, 132, 281
- Schilke, P., Groesbeck, T. D., Blake, G. A., & Phillips, T. G., 1997, 108, 301
- Schoier, F. L., van der Tak, F. F. S., van Dishoeck, E. F., Black, J. H. 2005, *A&A* 432, 369
- Sempere, M. J., Cernicharo, J., Lefloch, B., Gonzalez-Alfonso, E., Leeks, S., 2000, *ApJ*, 530,123
- Simpson, J. P., Rubin, R. H., Erickson, E. F. and Haas, M. R., 1986, *ApJ*, 311, 908
- Stacey, G. J., Kurtz, N. T., Smyers, S. D., & Harwit, M., 1983, *MNRAS*, 202, 25
- Stacey, G. J., Kurtz, N. T., Smyers, S. D., Harwit, M., et al., 1982, *ApJ*, 257, 37
- Stacey, G. J., Smyers, S. D., Kurtz, N. T., & Harwit, M., 1983, *ApJ*, 265, 7
- Sternberg, A., Dalgarno, A., 1995, *ApJ*, 99, 565
- Storey, J. W. V., Watson, D. M., Townes, C. H., Haller, E. E., et al., 1981, *ApJ*, 247, 136
- Sturm, E., Bauer, O.H., Lutz, D., et al. 1998, *ASP* 145, 161
- Sutton, E. C., Blake, G. A., Masson, C. R., & Phillips, T. G., 1985, *ApJ*, 58, 341
- Swinyard, B. M., Burgdorf, M. J., Clegg, P. E., Clegg, P. E., et al. 1998, *SPIE*, 3354, 888
- Taylor, S. D., Hartquist, T. W., Williams, D. A., 1993, *MNRAS*, 264, 929
- Tielens, A. G. M. & Hollenbach, D., 1985, *ApJ*, 291, 722
- Tielens, A. G. M. & Hollenbach, D., 1985, *ApJ*, 291, 747
- Townes, C. H., Genzel, R., Watson, D. M., Storey, J. W., 1983, *ApJ*, 269, 11
- Tucker, K. D., Kutner, M. L., Thaddeus, P., 1973, *ApJ*, 186,13
- Turner, B. E., Fourikis, N., Morris, M., Palmer, P., Zuckerman, B., 1975, *ApJ*, 198, 125
- Turner, B. E., 1989, *ApJ*, 70, 539
- van Dishoeck, E. F., Glassgold, A. E, Guelin, M., Jaffe, D. T, et al., 1992, *IAUS*, 150, 285
- van Dishoeck, E. F. , Wright, C. M., Cernicharo, J., Gonzalez-Alfonso, E., et al., 1998, *ApJ*, 502, 173
- Viscuso, P. J., Stacey, G. J., Fuller, C. E., Kurtz, N. T., Harwit, M. O., 1985, *BAAS*, 17, 570
- Watson, W.D. 1972, *ApJ*, 176, 103
- Watson, D. M., 1983, in Kessler M. F., Phillips, J. P., eds, *Noordwijk*, p.193
- Watson, D. M., Genzel, R., Townes, C. H., & Storey, J. W. V., 1985, *ApJ*, 298, 316
- Watson, W. D., Storey, J. W. V., Townes, C. H., Haller, E. E, et al., 1980, *ApJ*, 239, 129
- Wallace, P. T. & Clayton, C. A. 1996, *RV - Radial Components of Observer's Velocity*, *Starlink User Note* 78.8
- Werner, M. W., Hollenbach, D. J.; Crawford, M. K.; Genzel, R, et al., 1984, *ApJ*, 282, 81
- White, G. J., Araki, M., Greaves, J. S., Ohishi, M., Higinbottom, N. S., 2003, *A&A*, 407, 589
- Williams, D. A., & Hartquist, T. W., 1984, *MNRAS*, 210, 141
- Wilson, T. L., Gaume, R. A., Gensheimer, P., Johnston, K. J., 2000, *ApJ*, 538, 665
- Wootten, A., Boulanger, F., Bogey, M., Combes, F., et al., 1986, *A&A*, 166, 15
- Wootten, A., Mangum, J. G., Turner, B. E., Bogey, M., et al., 1991, *ApJ*, 380, 79
- Wright, C. M., van Dishoeck, E. F., Black, J. H., Feuchtgruber, et al., 2000, *A&A*, 358,689
- Wright, M. C. H., Plambeck, R. L., and Wilner, D. J., 1996, *ApJ*, 469, 216
- Ziurys, L. M., & McGonagle, D. 1993, *ApJ*, 89, 155